MODELING SAND RIPPLE EVOLUTION UNDER WAVE BOUNDARY LAYERS

By

ALLISON M. PENKO

A THESIS PRESENTED TO THE GRADUATE SCHOOL
OF THE UNIVERSITY OF FLORIDA IN PARTIAL FULFILLMENT
OF THE REQUIREMENTS FOR THE DEGREE OF
MASTER OF SCIENCE

UNIVERSITY OF FLORIDA

2007

To my family and friends.

ACKNOWLEDGMENTS

I gratefully acknowledge the Office of Naval Research for funding the Ripple DRI project, as well as ASEE and the National Defense Science and Engineering Graduate Research Fellowship Program for funding my education. I thank my supervisory committee for their support and mentoring and my fellow graduate students for their help and encouragement. Last, I thank my family and friends for their unwaivering encouragement and Aaron for being there for me every step of the way on this journey.

TABLE OF CONTENTS

ACKNOWLEDGMENTS 4

LIST OF TABLES 7

LIST OF FIGURES 8

ABSTRACT 10

CHAPTER

1 INTRODUCTION 11

1.1 General Introduction 11
1.2 Background 12
1.2.1 Types of Bedforms 13
1.2.2 Sediment Transport 14
1.2.3 Ripple Parameters 16
1.3 Literature Review 17
1.4 Research Problem 23

2 METHODOLOGY 28

2.1 Model Approach/Characteristics 28
2.2 Physics 28
2.2.1 Governing Equations 29
2.2.2 Non-dimensionalizing 36
2.2.3 Boundary and Initial Conditions 37
2.2.4 Input Parameters 38
2.3 Numerics 38

3 EXPERIMENTAL PLAN 44

3.1 Simulations 44
3.1.1 Ripple Amplitude Simulations 44
3.1.2 Ripple Wavelength Simulations 45
3.2 Experimental Data 46

4 RESULTS 51

4.1 Ripple Amplitude Simulations 51
4.1.1 Ripple Height 51
4.1.2 Ripple Shape 52
4.1.3 Suspended and Bed Load Transport 53
4.1.4 Advective, Settling, and Diffusive Fluxes 54
4.2 Ripple Amplitude Flow Velocity Simulations 56
4.2.1 Ripple Height 56
4.2.2 Suspended and Bed Load Transport 56

4.3 Two Ripple Wavelength Simulations . . . 57
4.3.1 Ripple Wavelength . . . 57
4.3.2 Ripple Height . . . 58
4.3.3 Suspended and Bed Load Transport . . . 58
4.4 One and Three Ripple Wavelength Simulations . . . 59
4.4.1 Ripple Wavelength . . . 59
4.4.2 Ripple Height . . . 59
4.4.3 Suspended and Bed Load Transport . . . 60
4.5 Flatbed Simulation . . . 60
4.5.1 Ripple Height . . . 60
4.5.2 Ripple Wavelength . . . 61
4.5.3 Suspended and Bed load Transport . . . 61
4.6 Three-Dimensional Simulation . . . 61
4.6.1 Ripple Height . . . 62
4.6.2 Suspended and Bed Load Transport . . . 62
4.7 Summary of Results . . . 62

5 SUMMARY . . . 85

5.1 Applicability . . . 85
5.2 Ripple Geometry Predictions . . . 85
5.2.1 Ripple Shape . . . 85
5.2.2 Ripple Height and Length . . . 85
5.2.3 Ripple Morphology . . . 86
5.2.4 Comparisons of Quasi-Two- and Three-Dimensional Simulations . . . 87
5.3 Summary of Contributions . . . 87
5.4 Future Research . . . 88

APPENDIX

A FLUX CALCULATIONS . . . 89

REFERENCES . . . 93

BIOGRAPHICAL SKETCH . . . 100

LIST OF TABLES

Table Page

3–1 Ripple amplitude simulation conditions. 47

3–2 Three-dimensional simulation conditions. 47

3–3 Ripple wavelength simulation conditions. 48

3–4 Model simulation parameters and laboratory data results. 49

4–1 Summary of the ripple height simulation results. 82

4–2 Summary of the ripple wavelength simulation results. 83

LIST OF FIGURES

Figure Page

1–1 Ripples in a sandy bed. 27

2–1 Mixture density and viscosity relationships. 40

2–2 Forces on a control volume in a concentrated sand bed. 41

2–3 The bed stiffness coefficient function. 41

2–4 Example of a three-dimensional initial bed state. 42

2–5 Staggered grid. 43

3–1 Initial bed states of the ripple amplitude simulations. 48

3–2 Initial bed state of the three-dimensional ripple amplitude simulation. 49

3–3 Initial bed states of the ripple wavelength simulations. 50

4–1 Snapshots in time of the ripple amplitude simulations. 63

4–2 Time evolution of the maximum ripple height in the ripple amplitude simulations. 64

4–3 Ripple slope plots of the ripple amplitude simulations. 65

4–4 Instantaneous and cumulative averaged bed and suspended load fluxes for the ripple amplitude simulations. 66

4–5 Instantaneous and cumulative averaged advective, diffusive, and settling fluxes for the ripple amplitude simulations. 67

4–6 Time, x-, and y-averaged flux plots for the ripple amplitude simulations. 68

4–7 Snapshots in time of the ripple amplitude simulations with varying maximum free-steam velocities. 69

4–8 Time evolution of maximum ripple height in the ripple amplitude simulations with varying maximum free-steam velocities. 70

4–9 Instantaneous and cumulative averaged bed and suspended load fluxes for the ripple amplitude simulations with varying maximum free-steam velocities. 71

4–10 Snapshots in time of the two ripple wavelength simulations. 72

4–11 Time evolution of maximum ripple height in the ripple wavelength simulations. . 73

4–12 Instantaneous and cumulative averaged bed and suspended load fluxes for the two ripple wavelength simulations. 74

4–13 Snapshots in time of the one- and three-ripple wavelength simulations. 75

4–14 Time evolution of maximum ripple height in the one- and three-ripple wavelength simulations. 76

4–15 Instantaneous and cumulative averaged bed and suspended load fluxes for the one- and three-ripple wavelength simulations. 77

4–16 Snapshots in time of the flatbed simulation. 78

4–17 Time evolution of maximum ripple height in the flatbed simulation. 79

4–18 Instantaneous and cumulative averaged bed and suspended load fluxes for the flatbed simulation. 80

4–19 Snapshots in time of the three-dimensional simulation. 81

4–20 Time evolution of ripple height in the three-dimensional simulation. 82

4–21 Instantaneous and cumulative averaged bed and suspended load fluxes for the three-dimensional simulation. 84

A–1 Ripple profile and horizontally averaged concentration plots. 91

A–2 Bed load layer and mesh grid. 92

Abstract of Thesis Presented to the Graduate School
of the University of Florida in Partial Fulfillment of the
Requirements for the Degree of Master of Science

MODELING SAND RIPPLE EVOLUTION UNDER WAVE BOUNDARY LAYERS

By

Allison M. Penko

May 2007

Chair: Donald N. Slinn
Major: Coastal and Oceanographic Engineering

A live-bed sediment transport and ripple morphology model is presented. An existing sheet flow mixture model is modified and its applicability to a highly concentrated, lower flow (Shields parameters less than 0.5), ripple regime is tested. Twelve simulations are presented with varying flow conditions and initial bed topographies to determine if the bed state will equilibrate to a predicted steady-state ripple geometry. The model is tested under a range of Reynolds number flows and bed states. It is found to predict ripples with similar shapes, heights, and lengths to those found in the laboratory and field. The dominant mechanism of ripple evolution is also analyzed. It is determined that ripple evolution in laminar and turbulent flow regimes occurs through bed load sediment transport. With experimental verification, the proposed mixture model has the potential to provide useful information on the dynamics of the flow, sediment transport, and ripple morphology.

CHAPTER 1
INTRODUCTION

1.1 General Introduction

Ripples have many impacts on the environment. Their length scales range from millimeters to meters, depending on the flow and sediment environment, affecting small-scale sediment transport to large-scale beach erosion. Even after much published research dating back as far as 1882 on ripples and the sediment transport over them, a better understanding of the dynamics of ripple development and the feedback between fluid-sediment interaction is still needed. A live-bed, three-dimensional model that predicts both suspended and bed load transport as well as ripple morphology has not been developed until now. Present models are limited in their capabilities. Some only describe one particular mode of sediment transport or are specific to a single flow regime or sediment parameter. While these models are useful in estimating net transport rates and providing insight to the modeled process or regime, they are unable to explain the physics of the natural system. Few three-dimensional models correctly simulate the flow together with accurately predicting ripple shape and size. Models that do not resolve small-scale processes, but instead approximate them with closure schemes, can introduce new complexities. Historically, there remains a measure of disagreement between the modeled results and field measurements (Sections 1.3 and 1.4).

Ripples are influential because they affect the near-bed turbulence and the boundary layer structure of the flow. The geometric properties and morphologic behaviors of sand ripples on the inner shelf can significantly impact sediment transport, bottom friction, and the acoustical properties of the seabed. For example, ripple migration is a significant mechanism of coastal sediment transport, influencing beach erosion and scour around objects. The bottom friction experienced by mean ocean currents, the damping effects felt by waves, and the quantity of suspended and bed load transport grows with increased bottom roughness that occurs due to the order of magnitude difference between grain size

and ripple height. Therefore, when ripples are present on the sea floor (Figure 1–1), the bottom roughness must be parameterized by the ripple height instead of the sediment size. Bedform properties, including height, wavelength, orientation, slope, shape, and grain size, affect the acoustic penetration and scattering characteristics of sonar. These effects become particularly important when acoustic sonar is used to search for buried objects (e.g., mines) under the seabed. A lack of sufficient information on ripple geometry provides an explanation for the missed detection of objects buried under the sea floor (Piper et al., 2002). Schmidt and Lee (1999) claim that the spectral characteristics of ripple fields are associated with a reverberation environment, which is highly sensitive to both the frequency and insonification aspect relative to the ripples.

We have developed a three-dimensional model using an approach that has never before been applied to the modeling of ripple evolution. The model allows for the prediction of ripple morphology and the hydrodynamics of the resulting flow. The model presented produces ripples similar to those seen in nature and allows for the examination of the dynamics of the flow, ripple formation, and ripple evolution. The properties that can be analyzed include the time-dependent concentration and velocity fields, the ripple height, length, shape, and migration. The information obtained from the model about the hydrodynamics and sediment transport over ripples can contribute to the overall understanding of the role of ripples in coastal morphology.

1.2 Background

Ripples form in many different environments and have a variety of characteristics. The bedform type depends on the strength and nature of the flow. A steady current, tidal current, waves, or a combination of all three will influence the size, shape, and orientation of the bedforms. The nonlinear complexities of the flow present challenges in predicting ripples, and much research has been done examining bedforms under different flow regimes (e.g., Bagnold, 1946; Sleath, 1984; Wiberg and Harris, 1994; Nielsen, 1992).

1.2.1 Types of Bedforms

Three of the most common types of bedforms are dunes, megaripples (or anti-dunes), and ripples. Dunes are irregular sandwaves formed under current action (i.e., in natural streams). They are generally triangular in shape with a mildly sloped upstream surface and a downstream slope approximately equal to the angle of repose. The flow over them separates at the crest and reattaches in the trough as they migrate downstream (Fredsøe and Deigaard, 1992). A megaripple, or anti-dune, is a large, round-crested, unstable ripple with a wavelength ranging from 1 m to 10 m, and a height from 0.1 m to 1 m. Their scales of evolution range from hours to days. Unlike dunes, anti-dunes can move upstream, with sand accumulating on the upstream face and eroding on the downstream slope. They form under energetic oscillatory flows and have irregular vortex shedding and unpredictable migration.

Ripples are the most common bedforms and are the focus of this research. Their wavelengths (λ) and heights (η) vary from 0.1 m to 1.0 m, and 0.01 m to 0.1 m, respectively. Their timescales of evolution can range from seconds to hours. Ripples can be wave- or current-generated, or a combination of both. Bagnold (1946) classified wave-generated ripples into two groups: rolling-grain ripples and vortex ripples. Rolling-grain ripples form first on an initially flat bed under low wave action. They are generally formed by oscillating waves creating a circular streamline path of flow. The orbital motion tends to push sediment up from a low to a high point on the bed. As the rolling-grain ripples grow, their height causes the boundary layer flow to separate behind the crest of the ripple and vortices are formed. The rolling-grain ripples are now transitioning into vortex ripples. Vortices carry sediment from the trough of the ripple up to the crest. Vortex ripples are usually two-dimensional and can be caused either by rolling-grain ripples already present or an obstruction on the sea floor such as a rock or shell. They can migrate slowly due to wave asymmetry, but not to the degree of current-generated ripples.

Current-generated ripples exist in rivers, estuaries, and the sea. They generally have a gentle upstream slope and a steep lee slope. The ripples migrate slowly downstream and can respond quickly to changes in the current strength and direction. They are usually three-dimensional with irregular geometries.

Ripples generated from both waves and currents have a combination of the properties mentioned previously. The strength and the relative angle between the waves and current influence the ripple characteristics. If the direction of the waves and currents are parallel, the ripple pattern is mainly two-dimensional. When the wave and current directions are perpendicular or a large angle apart, the ripple pattern is primarily three-dimensional (Nielsen, 1992, pg. 143-145; Sleath, 1984, pg. 169).

There are two more classifications within the wave-generated ripple category: orbital and anorbital. Orbital ripples have wavelengths proportional to the near-bed wave orbital diameter and heights greater than the wave boundary layer thickness. Ripples in a more energetic wave environment can have wavelengths independent of the wave orbital diameter and instead are proportional to the grain-size diameter. These are anorbital ripples. Orbital ripples predominately form in the laboratory, whereas anorbital ripples are generally found in the field (Wiberg and Harris, 1994).

1.2.2 Sediment Transport

Sediment transport is the mechanism from which bedforms evolve and migrate. The incipient motion of grains occurs when the mobilizing forces exceed some critical value. At this point, the stabilizing forces are not strong enough to hold the grains in place and the sediment starts to move. The modes of sediment transport are generally separated into three categories: bed load, suspended load, and wash load. Bagnold (1956) defines bed load as sediment that is supported by intergranular forces and is in almost continuous contact with the bed. Bed load is characterized by grains rolling or sliding over the bed. He identifies suspended load as sediment supported by fluid drag that is maintained in suspension by fluid turbulence. Wash load is very dilute suspended

sediment concentrations of fine particulates. In this work, we concentrate primarily on bed and suspended load.

Many methods exist to separate bed from suspended load when studying sediment transport. Einstein (1950) states that bed load is any moving sediment in the layer from the stationary bed up to two grain diameters above the bed. Fredsøe and Deigaard (1992) defined bed load as the layer with a volumetric bed concentration greater than 35% but less than 65% (fully packed sand). Because a grain can be supported by both intergranular forces and fluid drag at any given time, a distinction between bed and suspended load is virtually immeasurable in the laboratory and field. In this research, bed load is defined as part of the total load that moves below a chosen height above the stationary bed (see Appendix A for details). In general, bed load is within five grain diameters of the stationary bed, coinciding with concentrations of approximately 30%; and the stationary bed is typically designated as having a volumetric concentration of 60% or greater.

Suspended load transport over ripples is caused mainly by sediment being transported by vortices that form above the ripple lee slope. This process happens through two mechanisms. First, sediment is entrained in the vortex structures that are generated by the flow separation at the ripple crest. The second mechanism is the convection of the suspended sediment trapped in the vortices. The vortices are no longer clearly defined structures; therefore, the suspended sediment they contain is dispersed and convected by the mean flow (Sleath, 1984, pg. 266-269). Suspended sediment gets advected to a height $O(\eta)$ above the ripple (van der Werf et al., 2006). This convection process, as well as diffusion and gravity, are mechanisms that can cause ripple growth or decay. When the deteriorating forces are in balance with the growing forces, the ripple is in equilibrium for those specific conditions.

1.2.3 Ripple Parameters

Some important sediment transport and ripple morphology parameters include the mobility number, ψ, friction factor, f_w, wave orbital excursion, a, Shields parameter, θ, and the period parameter, χ. The mobility number (Equation 1–1) is a ratio of the disturbing forces to the stabilizing forces on a sediment particle under waves. It is a measure of a sediment particle's tendency to move due to wave action.

$$\psi = \frac{(a\omega)^2}{(s-1)gd} \tag{1–1}$$

where a is the wave orbital excursion (Equation 1–2), ω is the radial frequency (Equation 1–3), s is the specific gravity of the sediment (for quartz sand $s = 2.65$), and d is the median grain size diameter.

$$a = \frac{U_o T}{2\pi} \tag{1–2}$$

$$\omega = \frac{2\pi}{T} \tag{1–3}$$

where T is the period and U_o is the maximum free-stream velocity of the flow oscillation. A second parameter used to measure incipient motion is the Shields parameter (Equation 1–4). It is also a ratio of the disturbing to stabilizing forces.

$$\theta = \frac{u_*^2}{(s-1)gd} \tag{1–4}$$

where

$$u_* = \sqrt{\frac{\tau}{\rho_f}} \tag{1–5}$$

where u_* is the friction velocity (Equation 1–5), τ is the bed shear stress, and ρ_f is the water density. The Shields parameter (Equation 1–6) can also be defined in terms of the mobility number (Equation 1–1) and a friction factor, f_w (Equation 1–7).

$$\theta = \frac{1}{2} f_w \psi \tag{1–6}$$

where

$$f_w = exp\left(5.213\left(\frac{2.5d}{a}\right)^{0.194} - 5.977\right), \tag{1–7}$$

which was proposed by Swart (1974) with a roughness of $2.5d$ and is valid for rough turbulent flow conditions.

Mogridge and Kamphuis (1972) claim that ripple geometry depends on a dimensionless parameter derived from the mobility number and the wave orbital excursion length, called the period parameter (Equation 1–8).

$$\chi = \frac{d}{(s-1)gT^2}. \tag{1–8}$$

1.3 Literature Review

Published research on ripples dates back as far as 1882, when Hunt (1882) described his observations of the ripple-mark in sand. Following soon after, Candolle (1883) stated that ripples form when two liquids of different viscosities come in contact with each other in an oscillatory manner; and Forel (1883) observed that initial ripple wavelengths formed on a flat bed are about half as long as the equilibrium wavelengths. The first published ripple experiments were performed by Darwin (1883). He rotated a circular tub filled with sand and water in an oscillating motion and discovered that ripples formed radially in the sand. He and Ayrton (1910) observed the vortices that are generated in the lee

of ripples and noted that they eroded ripple troughs and built up the crests. The work of Bagnold (1946) was the next major contribution to the field of ripple dynamics. He defined bedforms as "vortex" ripples after observing the separation of flow at the ripple crest and the formation of a vortex in the lee of the ripple. When the flow reverses, the vortex is ejected upwards, causing the sediment to become suspended. He also presented the hypothesis that the ripple length is proportional to the wave orbital excursion length. Other significant investigations on the occurrence, formation, and development of ripples include Costello and Southard (1981), Sleath (1976), and Sleath (1984).

Field observations are crucial for the characterization of morphologic phenomena (Blondeaux, 2001). Some of the first significant data sets of ripple observations include Inman (1957), Dingler (1974), and Miller and Komar (1980a). These data confirm the hypothesis that the ripple wavelength is proportional to the wave orbital excursion length. Other early laboratory experiments have also contributed to the understanding of ripple dynamics (e.g., Carstens and Neilson, 1967; Mogridge and Kamphuis, 1972; Lofquist, 1978; Miller and Komar, 1980b). Empirical expressions to predict ripple height, wavelength, and steepness under different flow conditions have been formulated from laboratory and field measurements. The ripple predictor of Nielsen (1981) is one of the most well-known and verified. He developed formulas for ripple height, wavelength, and steepness under different flow conditions. Separate expressions are used for laboratory and field ripples (Section 3.2). Grant and Madsen (1982) used flume data of ripple spacing and height to develop general expressions for ripple height and steepness. A ripple predictor presented by Vongvisessomjai (1984) determines the geometry based on the grain size diameter and the period parameter, χ (Equation 1–8). Then, Mogridge et al. (1994) and Wiberg and Harris (1994) each presented a ripple predictor model. Mogridge et al.'s model predicted maximum ripple wavelength. Wiberg and Harris' model is more specific in its prediction of ripple geometry. The predictor is based on the type of ripple (orbital or anorbital), mean grain size, and the wave orbital excursion length. Unlike Nielsen's

method, the general expressions are applicable to both laboratory and field ripples. Much research has been done to examine and expand the validity of these ripple predictor methods. Li and Amos (1998) compared the methods of Grant and Madsen (1982) and Nielsen (1981) and proposed a modified expression that incorporates the enhanced shear velocity at the ripple crest. O'Donoghue and Clubb (2001) performed oscillatory flow tunnel experiments for field-scale ripples and applied the data to four existing ripple predictors. The comparison of the results of the Nielsen (1981), Mogridge et al. (1994), Vongvisessomjai (1984), and Wiberg and Harris (1994) methods to the experiments yields the author's recommendation of the Mogridge et al. (1994) model for the prediction of ripple geometries under field-scale oscillatory flows. Doucette (2002), Hanes et al. (2001), and Chang and Hanes (2004) found that the Nielsen (1981) method was the most accurate for predicting ripple wavelength when compared with their field observations of ripple height, length, and sediment compositions. Other modifications to the Nielsen (1981) equations have also been proposed (e.g., Faraci and Foti, 2002; Grasmeijer and Kleinhans, 2004; O'Donoghue et al., 2006; Williams et al., 2004).

In addition to examining ripple geometries, much work has also investigated the flow dynamics over ripples. Blondeaux (1990) predicted the conditions and characteristics for ripple formation under laminar flow. Later in 1990, Vittori and Blondeaux extended the work by performing a weak nonlinear analysis and included nonlinear terms into the model. They derived an amplitude equation that described the time development of the height of the fastest growing bottom perturbation near the critical conditions. The parameter space was divided into three separate regions: a region of low mobility numbers, a region in equilibrium but no flow separation, and a large oscillation region. The bed is stable in the low mobility number region. Rolling-grain ripples are the steady-state condition in the equilibrium region. The model is no longer valid in the large oscillation region due to the nonlinear dynamics of the flow. Foti and Blondeaux

(1995) extended the model into the turbulent regime by performing a linear stability analysis of a flat sandy bottom subject to oscillatory flow.

More recently, Faraci and Foti (2001) performed laboratory experiments to show that the rolling-grain ripples formed from a flat bed are only a transition to steady-state vortex ripples. They also determined that the bottom roughness must be parameterized by the ripple height, not the grain size diameter when ripples are present on the sea floor. Equilibrium ripples were closely investigated by Doucette and O'Donoghue (2006). They performed laboratory experiments to measure full-scale ripple profiles (up to 1.6 m in length). Ripples formed from flat beds and transient ripples were studied and the results were used to formulate an empirical relationship to predict ripple height evolution.

The history of sediment transport models is extensive. Model domains range from one- to three-dimensions. Some models resolve the hydrodynamics at small-scales while others cover larger scales and approximate sub-grid scale processes using advanced techniques. Sediment transport modeling dates back to 1979 when Grant and Madsen (1979) described wave and current motions over a rough bottom with an eddy-viscosity model. Their model predicted the distorted flow over ripples. Trowbridge and Madsen (1984) then developed a time-varying eddy-viscosity model that related oscillating turbulent flow over ripples to steady turbulent flow. This relation allowed the one-dimensional boundary layer solutions to be approximated. In 1981, Longuet-Higgins numerically described oscillatory flow over ripples using a discrete-vortex model. He approximated the oscillatory flow over steep ripples by assuming that the sand-water interface in the wave bottom boundary layer is fixed. These early models were then replaced by convection-diffusion models. One-dimensional convection-diffusion models (e.g., Nielsen, 1992; Lee and Hanes, 1996) account for small- and large-scale sediment mixing with an eddy-diffusivity model. Nielsen employs a time-invariant, vertically uniform, eddy-diffusivity profile, whereas Lee and Hanes uses the eddy-diffusivity model of Wikramanayake (1993) and Nielsen's (1992) pick-up function. Ribberink

and Al-Salem (1995) and Dohmen-Janssen et al. (2001) presented one-dimensional models with mixing lengths to calculate the suspended load in unsteady flow over a plane bed modeled with an enhanced bed roughness. Turbulence is modeled with an eddy-diffusion proportional to the eddy-viscosity used in the moment equation. Another notable sediment transport model is that of Li and Amos (2001). Their one-dimensional numerical model, SEDTRANS, predicts bed and suspended load transport rates, bedform development, and boundary layer parameters under wave, current, and combined flows for cohesive and non-cohesive sediments. It uses combined wave and current boundary layer theories (Grant and Madsen, 1986) to determine the near-bed velocity profiles and solves the time-dependent bed roughness with ripple predictors.

The most common approach in resolving the turbulent vortices over rippled beds is using turbulence closure schemes. The two most common turbulence closure schemes are the $k - \epsilon$ model and the $k - \omega$ model. The $k - \omega$ model has been found to handle regions of adverse pressure gradients better than the more familiar $k - \epsilon$ model (Guizien et al., 2003). Models incorporating the $k - \omega$ turbulence closure scheme include Wilcox (1998), Andersen (1999), Andersen et al. (2001), and Chang and Hanes (2004). Both Wilcox and Chang and Hanes solve the Reynolds Averaged Navier-Stokes (RANS) equations, whereas Andersen (1999) employs a Boussinesq approach. Andersen et al. (2001) uses a mass transport function to determine ripple evolution. Trouw et al. (2000), Eidsvik (2004), and Ji et al. (2004) employ $k - \epsilon$ turbulence schemes for their two-dimensional sediment transport models.

Three alternative methods for modeling sediment transport are presented in Hara et al. (1992), Hansen et al. (1994), and Andersen (2001). Hara et al. (1992) numerically solves the Navier-Stokes equations using a series method expanded to very high powers of ripple slope. It is valid for flows with small to moderately large Reynolds numbers and confirms the presence of oscillating vortices high above the Stokes boundary layer. In Hansen et al. (1994), a discrete vortex and Lagrangian model is used to describe the

two-dimensional sediment concentration fields over ripples. The discrete vortex model simulates the flow with a "cloud-in-cell" concept and the Lagrangian model tracks the individual particles. Andersen (2001) presents an interesting approach for modeling ripple evolution by treating the ripples as "particles." Each "particle" is governed by an equation of motion. The interactions between the "particles" and their migration therefore can be examined.

Continuous progress is being achieved in the areas of hydrodynamics, sedimentology, and bedform morphology, allowing for constant improvements in sediment transport and coastal morphology models. Three-dimensional models have only recently been possible due to the growing knowledge of flow dynamics and the advances in computer technology. Studies now show (e.g., Blondeaux, 2001; Blondeaux et al., 1999; Scandura et al., 2000) that vortex dynamics are highly three-dimensional and therefore should be examined in three-dimensions for a more complete understanding. Watanabe et al. (2003) developed a three-dimensional large-eddy simulation (LES) model that investigated moderate Reynolds number oscillatory flows over ripples. Zedler and Street (2006) presented a highly resolved three-dimensional LES model that solves the volume filtered Navier-Stokes equations. It includes an advection-diffusion equation with a settling term for suspended sediment and calculates the three-dimensional time-dependent velocity, pressure, and sediment concentration fields over long-wave ripples. The effect of ripples on boundary layer flow was examined by Barr et al. in 2004. They compared turbulence levels and dissipation rates of oscillatory flows over rippled and smooth beds. The three-dimensional, direct numerical solver (DNS) model allowed for the examination of boundary layer dynamics over ripples.

A completely different approach taken in sediment transport modeling involves treating the sediment and water phases as a continuous media with a varying viscosity. Einstein published the idea of an effective viscosity for particles in a fluid in 1906. He found that a mixture of particles and fluid behaves like a pure fluid with its viscosity

increased. Atkin and Craine (1976) then formalized a general review of the continuum theory for mixtures. Around the same time, Soo and Tung (1972), Soo (1978), and Drew (1975) analyzed the dynamics of the particulate phase. Drew (1975) applied turbulence averaging and mixing length theory to obtain the resulting Reynolds stresses. He included gravity, buoyancy, and linear drag forces. McTigue (1981) and Drew (1983) developed governing flow equations for the mixture of particles in fluid. Diffusion is modeled by averaging the fluid-particle interaction terms (including pressure gradients and drag forces) in the momentum balances. The turbulent fluctuations of the velocities and concentrations are accounted for with a decomposition and averaging scheme. Subia et al. (1998) numerically models suspension flows by incorporating Phillips et al.'s (1992) continuum constitutive equation describing the diffusive flux. The method includes a shear-induced migration model and a varying viscosity relationship. Recently, Hsu et al. (2004) proposed a sediment transport model under fully developed turbulent shear flows over a mobile bed. The model employs a Eulerian two-fluid approach to each phase and includes closure schemes for fluid and sediment stresses. There are many different approaches to sediment transport and coastal morphology modeling. This literature review is not exhaustive but includes several of the more relevant works to this research.

1.4 Research Problem

An accurate three-dimensional, hydrodynamic model of sediment transport and ripple morphology did not previously exist. Current ripple predictors include the effect of sediment transport on ripples through a roughness length scale, not from the actual flow dynamics and concentration field. Most existing sediment transport models approximate the Reynolds stress, and therefore do not completely resolve the flow field. The assumptions and approximations in these models can lead to inaccurate predictions of sediment transport. It is also unknown which parameters and mechanisms have the most significant effects on sediment transport. A realistic model of ripple geometry and flow dynamics under a range of conditions is necessary for a better understanding of sand

ripples. This research focuses on developing a tool that can provide information about the morphologic properties of ripples.

There are discrepancies between existing ripple predictor methods, even with much analysis of their validity (Doucette, 2002; Grasmeijer and Kleinhans, 2004; O'Donoghue and Clubb, 2001; Li and Amos, 1998). The results still depend on the type of data used for comparison (e.g., Faraci and Foti, 2002; Khelifa and Ouellet, 2000; O'Donoghue et al., 2006). Existing methods may not be reliable enough to obtain accurate detailed information about the dynamics of the flow because of approximations or assumptions made and/or empirical relations.

One-dimensional vertical (1DV) models can be based on eddy-viscosity and mixing length assumptions or have a more complete two-phase flow formulation. Eddy-viscosity models are derived from simple flow conditions and are therefore inadequate in modeling complex flows. Davies et al. (1997) compared four different 1DV models to determine if they successfully predicted suspended sediment concentration profiles. They found that the eddy-diffusivity models were incapable of predicting the convective or pick-up events during flow reversal. Phase lags between the measured and computed suspended sediment concentration profiles were also observed in the upper part of the boundary layer. Mixing length models (e.g., Ribberink and Al-Salem, 1995; Dohmen-Janssen et al., 2001) are specific to certain flow conditions since the mixing lengths are determined from experimental data based on local quantities. Some one-dimensional models restrict their predictions to a particular phenomenon, such as the boundary layer profile. While these models provide simple solutions and insight to the isolated process, they cannot contribute to the understanding of the interactions between processes. Lee and Hanes (1996) found that their convection-diffusion model is somewhat limited in its range of applicability. They determined that pure diffusion models work well under high energy conditions, whereas pure convection models work well under low energy conditions. However, a combined convection-diffusion model did not perform better than a pure convection

model under low energy conditions. The parameterization of ripples with a bed roughness coefficient oversimplifies sediment transport models by approximating the effects of the bed topography. The bed roughness predictions are important because a small change in the bedform dimensions has a large effect on the computed transport (Davies et al., 2002).

Models utilizing turbulence closure schemes to approximate small-scale processes can be inaccurate and problematic. Chang and Scotti (2004) found that the RANS equations are not adequate to model sediment suspension and transport in the ripple regime. This deficiency can possibly be attributed to: the altering of the turbulent flow properties in the presence of suspended sediment, the insufficiencies in turbulent sediment flux modeling, or an inaccurate representation of the concentration bottom boundary condition. They also found an underestimation of the Reynolds stress in the lee of the ripple, an overestimation of the vertical oscillation amplitude, and a necessity to tune parameters to the specific conditions of the simulation. From these results, Chang and Scotti (2004) concluded that the entire turbulent flow needs to be modeled correctly in order to accurately predict sediment transport. Additionally, two-dimensional models do not include the three-dimensionality of vortex formation. Studies now show the importance of three-dimensional vortex structures in sediment suspension and transport (Blondeaux, 2001).

The alternative "particle" model of Andersen (2001) is only applicable to rolling-grain ripples and does not employ a live-bed. Therefore, new "grains" or ripples cannot enter the system.

Large-eddy simulation models allow the dynamics of the largest vortex structures to be explicitly simulated in the numerics, but the effects of small vortices on the flow are parameterized. Thus, the flow is not simulated in its entirety. In the three-dimensional LES model of Watanabe et al. (2003), the oscillatory flow amplitude is limited to small values because the computational domain length must be an integral number of wavelengths. Although the Zedler and Street (2006) model is three-dimensional, it

employs a quasi-two-dimensional vortex formation-ejection mechanism, which could affect the results of sediment pick-up in three-dimensions. It also assumes a dilute fluid, and therefore is not applicable in the highly concentrated sand bed region. The main limitation of the flow model of Barr et al. (2004) is the fixed bed. Therefore, the effects on the flow field from suspended sediment and the evolving ripple shape are neglected. The models of McTigue (1981), Subia et al. (1998), and Hsu et al. (2004) are fairly successful in modeling dilute flows, but are less able to model regions of high concentrations. Subia et al.'s model is similar to the model presented in this research, but does not include a live-bed morphology model.

There are many inadequacies in existing sediment transport and ripple morphology models. Current models have difficulties accurately predicting ripple evolution together with sediment transport. The presented mixture model resolves the large- and small-scale dynamics of the flow over a live-bed, predicting both the concentration and velocity fields in conjunction with the ripple morphology under oscillatory flow.

Figure 1–1. Three-dimensional ripples in a sandy flume at the O. H. Hinsdale Wave Research Laboratory at Oregon State University. Photograph taken by Allison Penko.

CHAPTER 2
METHODOLOGY

2.1 Model Approach/Characteristics

Traditionally in modeling sediment transport, the solid and liquid phases are modeled separately and coupled with empirically based estimates of the fluid-particle and the particle-particle stress interactions. This two-phase approach requires a minimum of eight governing equations to close the system. In addition, dilute and dense flows are usually modeled separately because of the differences in the physics involved. When modeling dilute flows, the particle-particle interactions are usually neglected and the fluid stresses are modeled using turbulence closure schemes. In densely laden flows, the particle stresses cannot be ignored and models using closure schemes for the stresses are currently being developed. The mixture model presented approaches the problem of sediment transport modeling by treating the fluid-particle system as a continuum consisting of two interacting materials, or phases. Some of the physics of the coupled system are then approximated with empirically based submodels. This method requires a constitutive equation expressing the total stress as functions of various fields. It includes three mixture momentum equations, an equation describing how the sediment moves within the mixture, and a mixture continuity equation. Using this approach to model sediment transport, we assume the two phases, sand particles and water, can be approximated by a mixture having a variable density and viscosity dependent on local sediment concentration.

2.2 Physics

The live-bed, three-dimensional, turbulent wave bottom boundary layer mixture model developed by Slinn et al. (2006) for sheet flow conditions has been adapted for sediment properties and flow regimes characteristic of the generation and morphology of bedforms. The model has previously shown to reasonably predict the suspended sediment concentration profiles at different wave phases for sheet flow conditions. The finite difference model is used to simulate the flow caused by realistic waves over a

three-dimensional, evolving bed shape in domains $O(10^3)$ cubic centimeters. It implements a control-volume scheme that solves for the time-dependent sediment concentration function and the mass and momentum conservation equations for the mixture to a second-order approximation in space and third-order accuracy in time. Both fluid-particle and particle-particle interactions are accounted for through a variable mixture viscosity, a concentration specific settling velocity formulation, and a stress induced, empirically calibrated, mixture diffusion term.

2.2.1 Governing Equations

The five governing equations for the mixture model include a sediment continuity, a mixture continuity, and mixture momentum equations. First, the properties of the mixture are defined. The mixture has a variable density and viscosity that depend on the local sediment concentration. The mixture density, ρ, is derived from the relation stating that the density of a mixture composed of n species is the sum of the bulk densities, $\bar{\rho_n}$, of each species:

$$\begin{aligned} \rho &= \sum_n \bar{\rho_n} \\ &= \sum_n C_n \rho_n \end{aligned}$$

where $\bar{\rho_n}$ is the ratio of the mass of species n to the total volume of the mixture, C_n is the concentration of species n, and ρ_n is the ratio of the mass of species n to the volume of species n. For a two-species mixture, $C_1 + C_2 = 1$, and therefore $C_2 = 1 - C_1$. Summing the concentrations and densities for a two-species mixture and substituting for C_2,

$$\begin{aligned} \rho &= C_1\rho_1 + C_2\rho_2 \\ &= C_1\rho_1 + (1 - C_1)\rho_2. \end{aligned}$$

For a two-species mixture of sediment in water, C_1 and ρ_1 are defined as the sediment concentration and density, respectively. C_2 and ρ_2 are defined as the concentration and density of water, respectively. The sediment-water mixture density, ρ, is shown in Equation 2–1.

$$\rho = C\rho_s + (1 - C)\rho_f \tag{2–1}$$

where ρ_s is the sediment density, ρ_f is the water density, and C is the concentration of sand particles in the mixture, ranging from 0% to 60%, which corresponds to fully packed sand. Therefore, $(1 - C)$ is the concentration of water in the mixture. Figure 2–1(a) is a plot of the mixture density versus local sediment concentration. The mixture viscosity, μ, is also a function of sediment concentration proposed by Leighton and Acrivos (1987) (Equation 2–2).

$$\frac{\mu}{\mu_f} = \left[1 + \frac{1.5CC_p}{C_p - C}\right]^2 \tag{2–2}$$

where μ_f is the fluid viscosity and C_p is the maximum packing concentration ($C_p = 0.615$ for random close packing of sand particles in water). Figure 2–1(b) compares the ratio of the mixture viscosity to the fluid viscosity with Hunt et al.'s (2002) analysis of Bagnold's 1954 experiments. The results show that the effect of high concentrations of particles in water can be parameterized by a bulk viscosity.

The first governing equation, the mixture continuity equation, is derived from the sum of the fluid and sediment phase continuity equations (Drew, 1983):

$$\frac{\partial(1 - C)\rho_f}{\partial t} + \frac{\partial(1 - C)\rho_f u_{fj}}{\partial x_j} + \frac{\partial C\rho_s}{\partial t} + \frac{\partial C\rho_s u_{sj}}{\partial x_j} = 0.$$

Rearranging, we obtain,

$$\frac{\partial}{\partial t}[C\rho_s + (1-C)\rho_f] + \frac{\partial}{\partial x_j}[C\rho_s u_{sj} + (1-C)\rho_f u_{fj}] = 0.$$

Note that the time derivative in the first term is the mixture density, ρ (Equation 2–1), and the spatial derivative in the second term is the mixture flux, the mixture density times the mixture velocity, u_j. Substituting for the two terms, the mixture continuity equation becomes

$$\frac{\partial \rho}{\partial t} + \frac{\partial \rho u_j}{\partial x_j} = 0. \tag{2–3}$$

The mixture momentum equation is also derived from the sum of the individual phase momentum equations resulting in

$$\frac{\partial \rho u_i}{\partial t} + \frac{\partial \rho u_i u_j}{\partial x_j} = -\frac{\partial P_M}{\partial x_i} + \frac{\partial \tau_{ij}}{\partial x_j} + F\delta_{i1} - \rho g \delta_{i3} + \frac{\partial P_P}{\partial x_i} \tag{2–4}$$

where P_M is the mixture pressure, τ_{ij} is the mixture stress tensor, F is the external driving force (Equation 2–8), g is the gravitational constant, and P_P is the particle pressure (described later in this section). Bagnold (1954) and others have determined that fluid-sediment mixtures may follow Newton's law of viscosity, therefore, τ_{ij} can be given by

$$\tau_{ij} = \mu \left[\frac{\partial u_i}{\partial x_j} + \frac{\partial u_j}{\partial x_i} - \frac{2}{3}\frac{\partial u_k}{\partial x_k} \right]. \tag{2–5}$$

The flow is driven by an external oscillating force, F, that approximates the oscillating velocity field induced by a surface gravity wave propagating over a seabed. It is described by the force from the wave minus an opposing force in the fully packed rigid bed.

$$F_{wave} = \rho_f U_o \frac{2\pi}{T} \cos \frac{2\pi}{T} t \tag{2–6}$$

$$F_{rigid} = \left(\frac{\bar{C}_x(z)}{C_m} \right)^{10} \rho_f U_o \frac{2\pi}{T} \cos \frac{2\pi}{T} t \tag{2–7}$$

$$F = F_{wave} - F_{rigid} \tag{2–8}$$

where U_o and T are the amplitude and period of the oscillation, respectively, $\bar{C}_x(z)$ is the averaged local concentration in the x-direction, and C_{max} is the maximum concentration of sediment. When the average concentration is approximately equal to the maximum concentration (i.e., in the sand bed), the high powered term is close to unity, and therefore the forcing, F, is approximately equal to zero. When the average concentration is less than the maximum concentration (i.e., in the water column), the high powered term becomes very small, and F equals F_{wave}. This formulation for the external force prevents "plug flow" in the model that could occur due to the periodic boundary conditions. Plug flow is the movement of the entire bed as a unit through the domain.

The sediment continuity equation (Equation 2–9) describes how the sediment moves within the mixture (Nir and Acrivos, 1990).

$$\frac{\partial C}{\partial t} + \frac{\partial C u_j}{\partial x_j} = -\frac{\partial C W_t}{\partial z} + \frac{\partial N_j}{\partial x_j} \tag{2–9}$$

where W_t is the concentration specific settling velocity and N_j is the diffusive flux of sediment (Equation 2–13).

Richardson and Zaki (1954) found that settling velocity can be calculated as a function of sediment concentration by

$$W_t = W_{t0}(1 - C)^q \tag{2–10}$$

where W_{t0} is the settling velocity of a single particle in a clear fluid and q is an empirical constant dependent on the particle Reynolds number, Re_p, defined as

$$Re_p = \frac{d\rho_f |W_{t0}|}{\mu_f} \tag{2–11}$$

where d is the grain size diameter. The empirical constant q is then defined by Richardson and Zaki (1954) as

$$q = \begin{cases} 4.35 Re_p^{-0.03} & 0.2 < Re_p \leq 1, \\ 4.35 Re_p^{-0.10} & 1 < Re_p \leq 500, \\ 2.39 & 500 < Re_p. \end{cases} \tag{2–12}$$

In the mixture model, the diffusive flux in Equation 2–9 is approximated by Leighton and Acrivos (1986). Sediment diffusion depends on collisional frequency, the spatial variation of viscosity, and Brownian diffusion such that

$$N = N_c + N_\mu + N_B \tag{2–13}$$

where N_c is the flux due to collisions, N_μ is the flux due to the variation of viscosity, and N_B is the flux to due Brownian diffusion. N_B is very small in comparison with the other terms and can therefore be neglected (Phillips et al., 1992). Leighton and Acrivos (1986) developed the expression for diffusive flux for sediment flow on an inclined surface that accounts for the flux due to collisions only. It includes a variable diffusion coefficient that is a function of particle size, concentration, and mixture stresses, and is given by

$$N_j = D_j \frac{\partial C}{\partial x_j} \tag{2–14}$$

where

$$D_j = d^2 \beta(\hat{C}) \left| \frac{\partial u_i}{\partial x_j} \right| \tag{2–15}$$

and where $\beta(\hat{C})$ is a dimensionless coefficient empirically determined and approximated by Leighton and Acrivos (1986).

$$\beta(\hat{C}) = \alpha \hat{C}^2 \left(1 + \frac{1}{2} e^{8.8\hat{C}} \right) \tag{2–16}$$

where $\hat{C}$ is the dimensionless concentration (Section 2.2.2) and α is an empirical constant. Leighton and Acrivos (1986) found α to be approximately 0.33 for larger Shields parameter values ($0.5 < \theta < 30$) and stated a likely underestimation of the diffusion coefficient with this value. In this research, all but one case has a Shields parameter value under 0.5. Testing the three-dimensional mixture model showed that $\alpha = 0.4$ best approximated the diffusion coefficient for smaller Shields parameters in the ripple flow regime.

The original sheet flow mixture model needed a modification in order to be applicable in a highly concentrated, lower flow regime conducive for sand ripple initiation and growth. In regions of high concentrations, the contact forces between the particles become significant. The intergranular forces cannot be represented simply by a shear stress, thus, a normal stress must be included. Consider a still bed with the sand particles at rest. Stress is transmitted from particle to particle at their points of contact. At these points, the stress is large. The stress will be equal to the surrounding fluid stress in areas where particles are not in contact with each other. In dilute mixtures, the ratio of contact area to total area is small and the contact stresses can therefore be neglected. However, in mixtures of high concentrations (i.e., the packed bed of a sand ripple), the contact stresses are significant and must be accounted for (Drew, 1983). This normal force resulting from particles being in contact with each other can be referred to as a particle pressure.

Figure 2–2 shows the forces on a control volume in the bed and the particle pressure opposing them. This resistance to pressure was necessary for a rigid bed.

The particle pressure force is represented in the model through a bed stiffness coefficient. The bed stiffness coefficient, B_s, acts as the particle pressure, opposing the forces on the mixture when the concentration is high. Figure 2–3 shows the function describing the bed stiffness coefficient for varying sediment concentrations. The shape of the function was modeled after Jenkins and Hanes (1998) calculations of particle pressure with respect to boundary layer height and the viscosity/concentration relationship (Figure 2–1(b)). The eighth power exponential function was chosen after much testing of the bed response to a range of function powers and coefficients. The bed stiffness function allows the forces on the mixture to be fully opposed when the concentration is greater than 57% by volume and only slightly opposed when the concentration of sediment is less than 57% but greater than 30%. Previous research (e.g., Fredsøe and Deigaard, 1992, pg. 218) states that the minimum bedload concentration (i.e., enduring contact region) is about 35% concentration by volume. Note the bed stiffness coefficient does not make the bed completely rigid, even at a volumetric concentration of 60% (a fully packed bed). Pore pressure and the spherical grain shape cause water to seep through the stationary grains, producing a small mixture velocity in the packed bed. Therefore, a completely stationary bed would not be representative of the physics in the packed bed region. The model approach retains this feature.

2.2.2 Non-dimensionalizing

The mixture model uses non-dimensional parameters in its calculations. The scaled parameters (denoted with a hat) are non-dimensionalized by the following:

$$
\begin{aligned}
\hat{x}_j &= \frac{x_j}{d} \\
\hat{t} &= \frac{t|W_{to}|}{d} \\
\hat{C} &= \frac{C}{C_m} \\
\hat{\rho} &= \frac{\rho}{\rho_f} \\
\hat{\mu} &= \frac{\mu}{\mu_f} \\
\hat{u}_j &= \frac{u_j}{|W_{to}|} \\
\hat{D}_j &= \frac{D_j}{|W_{to}|d} \\
\hat{P} &= \frac{P}{\rho_f |W_{to}|^2} \\
\hat{F} &= \frac{Fd}{\rho_f |W_{to}|^2}
\end{aligned}
$$

where ρ_f is the fluid density, C_m is the maximum concentration (0.6). Substituting in for the scaled variables, Equation 2–3, Equation 2–4, and Equation 2–9, become

$$\frac{\partial \hat{\rho}}{\partial \hat{t}} + \frac{\partial \hat{\rho}\hat{u}_j}{\partial \hat{x}_j} = 0, \tag{2–17}$$

$$\frac{\partial \hat{\rho}\hat{u}_i}{\partial \hat{t}} + \frac{\partial \hat{\rho}\hat{u}_i\hat{u}_j}{\partial \hat{x}_j} = -\frac{\partial \hat{P}_F}{\partial \hat{x}_i} + \frac{1}{Re_p}\frac{\partial \hat{\tau_{ij}}}{\partial \hat{x}_j} + \hat{F}\delta_{i1} - Ri\delta_{i3} + \frac{\partial \hat{P}_P}{\partial \hat{x}_i}, \tag{2–18}$$

and

$$\frac{\partial \hat{C}}{\partial \hat{t}} + \frac{\partial \hat{C}\hat{u}_j}{\partial \hat{x}_j} = -\frac{\partial \hat{C}\hat{W}_t}{\partial \hat{z}} + \frac{\partial}{\partial \hat{x}_j}\left(\hat{D}_j \frac{\partial \hat{C}}{\partial \hat{x}_j}\right), \tag{2–19}$$

respectively, where

$$Ri = \frac{(1-\hat{\rho})dg}{|W_{to}|^2}. \tag{2–20}$$

2.2.3 Boundary and Initial Conditions

The model is initialized with varying bed topographies ranging from a flat bed to multiple sinusoidal ripples with different heights and lengths. The desired initial bed is chosen for the simulation and described with a function. The model then sets all points according to the bed function to have a fully packed sediment concentration ($\hat{C} = 1$), and all grid points above the bed to have a concentration of zero. Initially, the mixture is at rest and all velocities are zero. Figure 2–4 shows an example of an initial concentration profile. The initial topography is slightly three-dimensional to break the symmetry of the problem and allow for the development of turbulent three-dimensional flow. The initial conditions are as follows:

$$\begin{aligned} \hat{C} &= f(x,y,z) = 1 \quad \text{as given in the model run input} \\ \hat{u_j} &= 0. \end{aligned}$$

The nature of the flow and the domain used allows for the implementation of periodic boundary conditions in the x- and y-directions. At the top of the domain, a free-slip boundary condition is used for the u and v velocities, and a no-gradient condition is imposed for the diffusion coefficient, D. The concentration field and the w velocity is zero at the top of the boundary. Equation 2–21 gives the special boundary condition for the

fluid pressure at the top of the domain necessary for the numerical implementation of the pressure projection method used in the model.

$$\frac{\partial \hat{P}}{\partial \hat{z}} = \frac{(\hat{\rho}\hat{w})^*}{\Delta t} \tag{2–21}$$

where $(\rho u_i)^*$ is equal to the integrated terms (with respect to time) of the mixture momentum equation that do not include pressure or the advanced velocity term.

There is fully packed sand at the bottom of the domain, therefore it is assumed that there is no movement, and no-slip boundary conditions are used for all the velocities. It is also assumed there is no concentration or diffusive flux at the bottom. The boundary conditions are summarized as follows:

Top			Bottom		
C	$=$	0	$\frac{\partial C}{\partial z}$	$=$	0
$\frac{\partial D}{\partial z}$	$=$	0	$\frac{\partial D}{\partial z}$	$=$	0
$\frac{\partial u}{\partial z}$	$=$	0	u	$=$	0
$\frac{\partial v}{\partial z}$	$=$	0	v	$=$	0
w	$=$	0	w	$=$	0
$\frac{\partial P}{\partial z}$	$=$	$\frac{(\rho w)^*}{\Delta t}$	P	$=$	$0.$

2.2.4 Input Parameters

The model input parameters establish the domain size, flow oscillation strength and frequency, grid size, grain size diameter, and length of simulation. From these inputs, the model determines all other variables including the time step and dimensionless parameters such as the particle Reynolds number. The model then solves for the velocities, concentration, and pressure using the procedure described in Section 2.3.

2.3 Numerics

A control volume approach on a three-dimensional staggered grid is taken to numerically solve Equations 2–17, 2–18, and 2–19. Figure 2–5 shows the staggered grid,

where circles represent concentration and pressure points and arrows represent momentum and velocity points. The shaded areas are ghost points. Turbulence is modeled directly with the equations because the grid spacing is smaller than the smallest-eddy length scale. Spatial derivatives are calculated using one-sided differences, resulting in second-order accuracy. The third-order Adams-Bashforth scheme is used to advance concentration and momentum in time, with explicit Euler and second-order Adams-Bashforth schemes used as starting methods.

No adjustments were made in the implementation of the control volume approach for the momentum equations, but non-traditional flux-conservative techniques were employed in the solution of the sediment continuity equation to ensure mass conservation, solution stability, and propagation of bed height as particles settle out. These techniques include the use of a harmonic mean that acts as a flux limiter and the use of a minimum diffusion coefficient that acts as a filter.

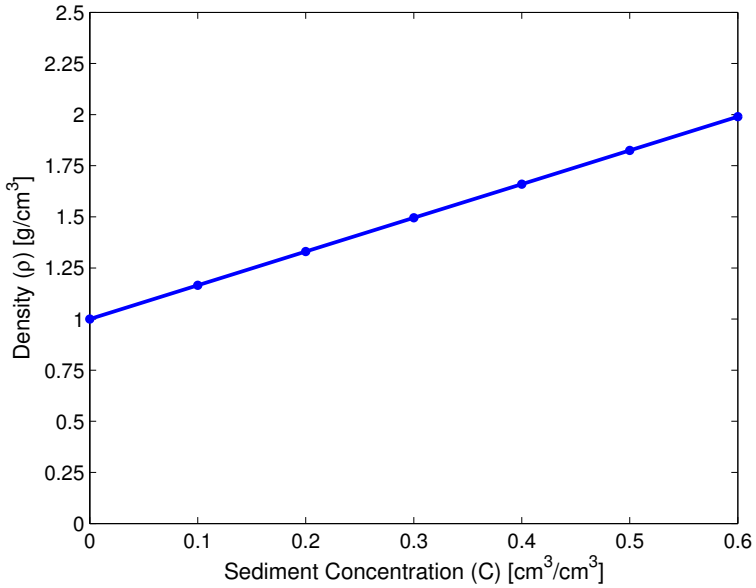

(a)

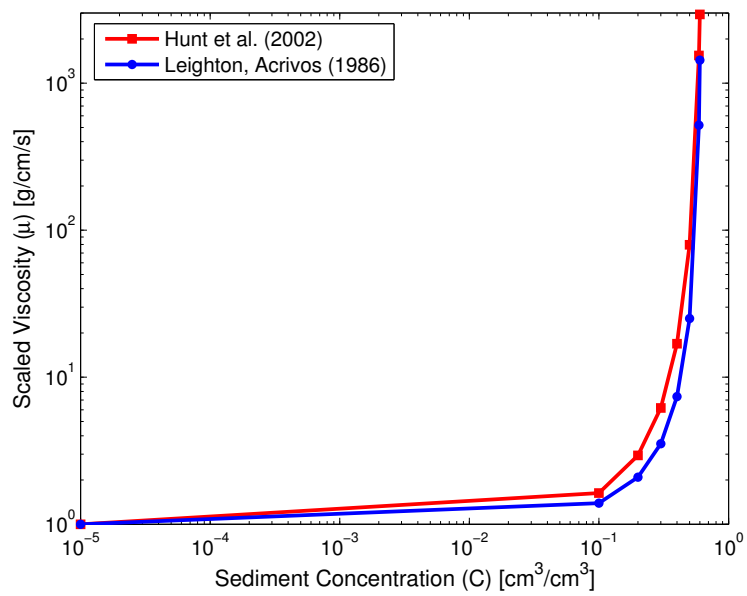

(b)

Figure 2–1. The (a) mixture density versus sediment concentration and (b) the ratio of the mixture viscosity to the fluid viscosity versus sediment concentration.

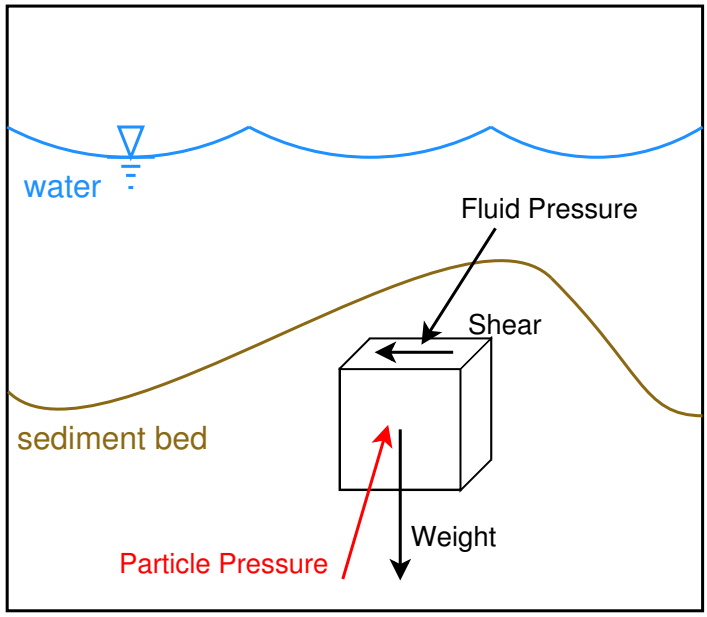

Figure 2–2. Forces on a control volume in a concentrated sand bed. The particle pressure opposes the sum of the shear stress, fluid pressure, and the weight of the sediment in the control volume.

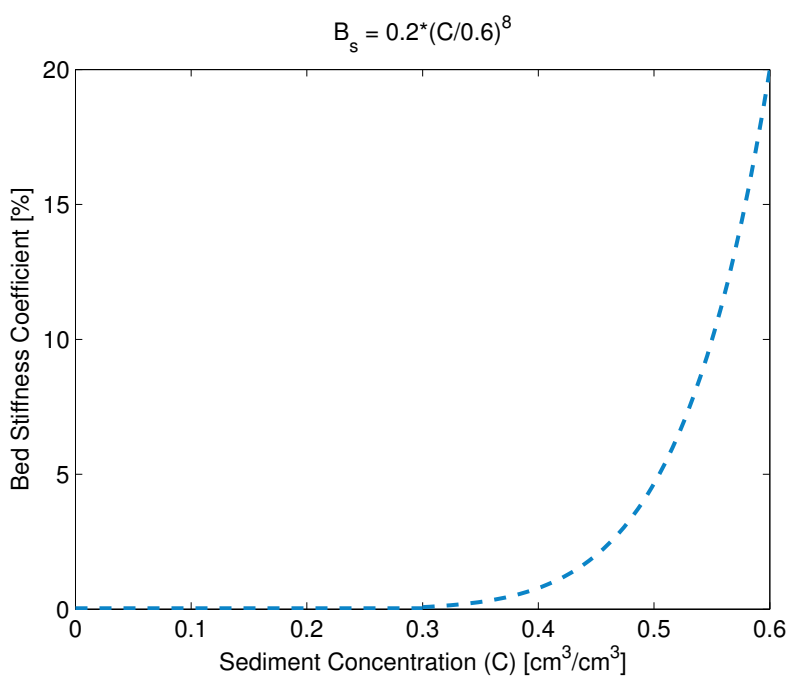

Figure 2–3. The bed stiffness coefficient function. The coefficient is zero until the sediment concentration is 30% by volume. B_s then increases as a polynomial function.

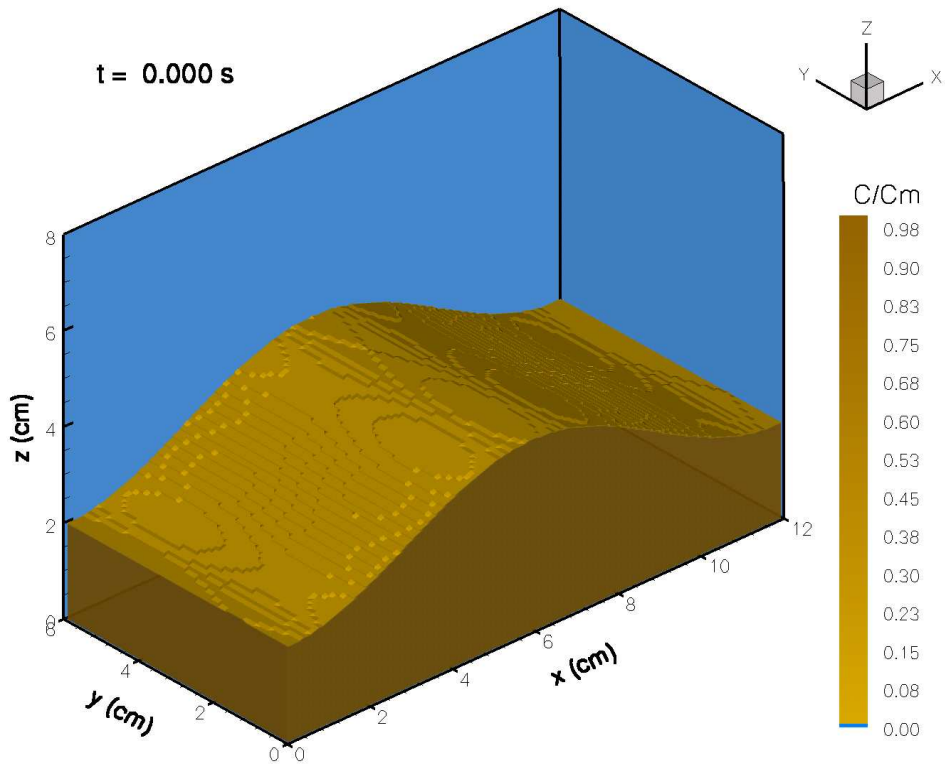

Figure 2–4. Example of a three-dimensional initial bed state. The height of the sinusoidal ripple varies in the x- and y-directions.

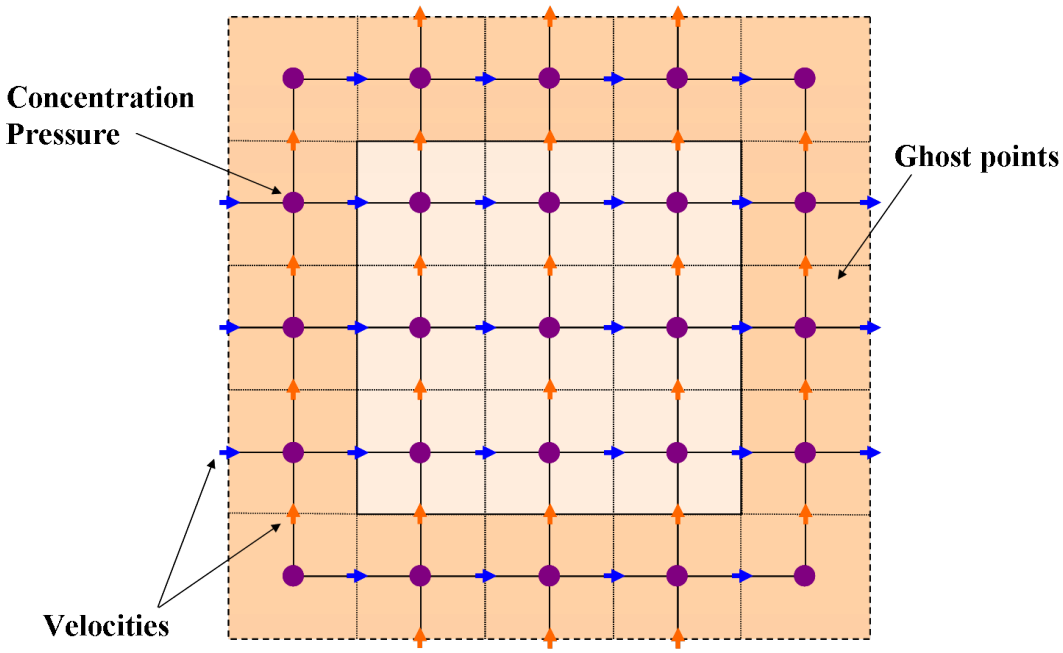

Figure 2–5. Staggered grid used in the control volume approach. The circles are points of concentration and pressure calculations, the arrows are velocity and momentum points of calculation. The outer-most points (shaded region) are ghost points.

CHAPTER 3
EXPERIMENTAL PLAN

3.1 Simulations

Simulations tested the model's capability to predict the steady-state ripple height and wavelength for various flow conditions. In most cases, the simulations were run until the ripple reached equilibrium, the limiting factor being the duration of the computations. Twelve different model simulations are presented out of over one-hundred cases tested. The cases demonstrate the model's ability to predict ripple shape under certain flow conditions. Eleven of the cases are quasi-two-dimensional and one is three-dimensional. The model is fully three-dimensional but very computationally expensive (about 75 days of CPU time for a 10 second three-dimensional simulation). The simulations are run in quasi-two-dimensions to approximate the model's three-dimensional behavior in a more reasonable amount of time (about one week). A quasi-two-dimensional simulation has full dimensions in the x- and z-directions, but has only two grid points in the y-direction. This reduction of grid points decreases the number of computations and ultimately reduces the computational time by a factor of about 32. Because the quasi-two-dimensional simulations showed the model was applicable to the ripple regime, equivalent three-dimensional simulations could be used for additional analysis. Each case tested whether or not the ripple amplitude and wavelength equilibrated to a steady-state height and length as determined by Nielsen (1981), which is further explained in Section 3.2.

3.1.1 Ripple Amplitude Simulations

Ripple amplitude simulations illustrate the model's ability to predict a ripple height near the expected equilibrium ripple height under different flow conditions. Table 3–1 describes the initial shape and flow conditions of each of the two-dimensional ripple amplitude simulations. The first three two-dimensional simulations were forced with the same flow having a maximum free-stream velocity of 40 cm/s and a 2 second period,

but were initialized with different ripple heights. Cases E11, E13, and E20, were forced with flows having 20 cm/s, 60 cm/s and 120 cm/s maximum free-stream velocities, respectively. Figure 3–1 shows the initial ripple states for each of the two-dimensional ripple amplitude simulations. The three-dimensional case is initialized with a ripple 2 cm in height subjected to an oscillatory flow with a maximum free-stream velocity of 40 cm/s and a 2 second period. Its initial ripple state is illustrated in Figure 3–2 and its simulation conditions are described in Table 3–2. All the simulations (including the ripple wavelength simulations, Section 3.1.2) include a sediment grain size of 0.4 mm. The horizontal length scale of the model is constrained in the ripple amplitude simulations because the periodic boundary conditions do not allow the ripple wavelength to change. Unlike the wavelength runs, only the change in ripple amplitude can be examined in these seven simulations.

3.1.2 Ripple Wavelength Simulations

Five simulations tested the model's ability to predict ripple wavelength in addition to ripple amplitude. Each simulation was forced with the same oscillatory flow and initialized with integral numbers and sizes of ripples as listed in Table 3–3. The first case, E05, is initialized with two slightly merged sinusoidal ripples in a domain appropriate for one wavelength of the associated steady-state ripple. Case E10 is the same as E05, but instead of two slightly merged ripples, two fully sinusoidal ripples were initialized. In case E08, a domain the length of two steady-state ripples was initialized with only one long ripple to test the model's ability to predict two ripples. Three ripples were initialized in case E09 in a domain the length of two steady-state ripples. Case E18 is initialized with a flat bed with just a small perturbation in the center of the domain. Figure 3–3 shows the initial states for each of these cases. Both the ripple wavelength and amplitude can be examined in these simulations because the periodicity does not prevent the wavelength from changing.

3.2 Experimental Data

Field and laboratory observations are crucial for the characterization of morphologic phenomena (Blondeaux, 2001). In this stage of research with the model, prior synthesis of the data is being used to test the model's applicability to the sand ripple regime. Nielsen's (1981) ripple predictor method was chosen to compare with the model output. He compiled laboratory data sets of regular waves over a sandy bed and collapsed the findings into formulas. The equations describe the heights and lengths of ripples in their equilibrium state in terms of the mobility number (Equation 1–1). The laboratory data included grain sizes ranging from 0.082 mm to 1.00 mm, and mobility numbers ranging from 0 to 230. Previous research has shown that Nielsen's method is one of the most accurate of the currently existing ripple predictor methods (O'Donoghue et al., 2006; Faraci and Foti, 2002; Grasmeijer and Kleinhans, 2004).

The formulas were used as a guideline to determine the model's ability to predict a steady-state ripple height and length under different flow conditions. For steady-state ripple height Nielsen determined the following:

$$\eta = \begin{cases} a(0.275 - 0.022\psi^{0.5}) & \psi < 156 \\ 0 & \psi > 156 \end{cases} \tag{3–1}$$

where a is the wave orbital excursion length described in Equation 1–2, and ψ is the mobility number (Equation 1–1). Table 3–4 lists the simulation parameters and formula results for the flow regimes simulated.

For small mobility numbers ($\psi < 20$), Mogridge and Kamphuis (1972) found that Equation 3–2 can describe steady-state ripple length for numerous flow periods, grain sizes, and densities.

$$\lambda = 1.3a \qquad \psi \leq 20 \tag{3–2}$$

Nielsen then expanded this formula by compiling ripple length data for mobility numbers ranging from 2 to 230. He formulated the equation for steady state ripple length is as follows

$$\lambda = a(2.2 - 0.345\psi^{0.34}) \qquad 2 < \psi < 230. \tag{3–3}$$

Nielsen's ripple predictor formulas are valid for the flow conditions tested in the simulations presented in this work, and are used as a test of the model's capability of predicting ripple geometry. Future work includes a comparison of the model results to concentration, velocity, and ripple morphology data.

Table 3–1. The ripple amplitude simulations and their conditions.

Run name	Initial bed shape	Initial ripple height (cm)	Initial ripple length (cm)	Domain height (cm)	Domain length (cm)	U_o (cm/s)	T (s)
E03	(1) sinusoidal ripple	1.0	12.0	8.0	12.0	40.0	2.0
DC05	(1) sinusoidal ripple	2.0	12.0	8.0	12.0	40.0	2.0
E04	(1) sinusoidal ripple	3.0	12.0	12.0	12.0	40.0	2.0
E11	(1) sinusoidal ripple	2.2	8.0	8.0	8.0	20.0	2.0
E13	(1) sinusoidal ripple	1.6	16.0	12.0	16.0	60.0	2.0
E20	(1) sinusoidal ripple	1.6	8.0	16.0	8.0	120.0	4.0

Table 3–2. The three-dimensional simulation (E14) conditions.

Run name	Initial bed shape	Initial ripple height (cm)	Initial ripple length (cm)	Domain height (cm)	Domain length (cm)	Domain width (cm)	U_o (cm/s)	T (s)
E14	(1) sinusoidal ripple	2.0	12.0	8.0	12.0	6.0	40.0	2.0

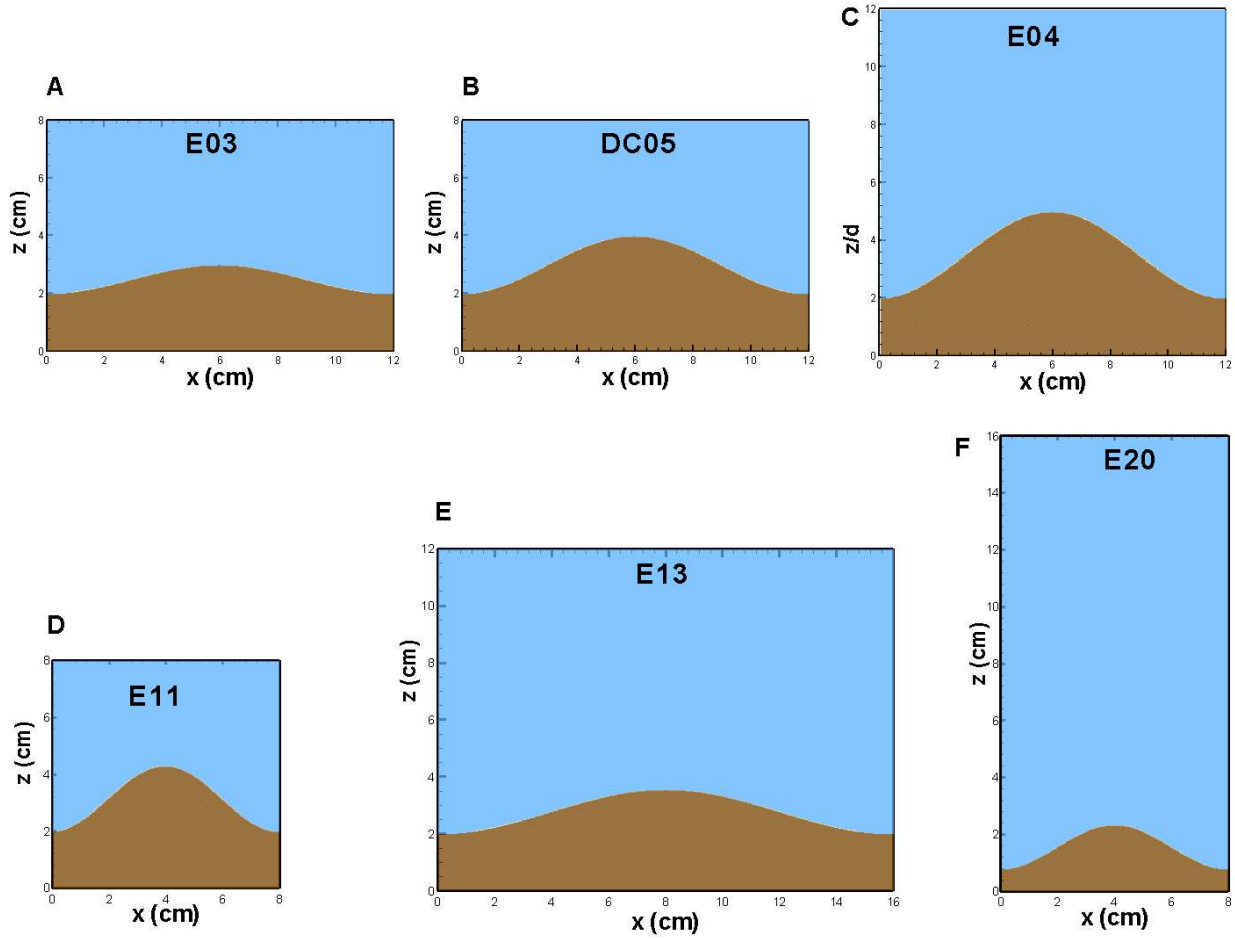

Figure 3–1. Initial bed states of the ripple amplitude simulations. (a) Case E03, (b) case DC05, (c) case E04, (d) case E11, (e) Case E13, and (f) case E20.

Table 3–3. The ripple wavelength simulations and their conditions.

Run name	Initial bed shape	Initial ripple height (cm)	Initial ripple length (cm)	Domain height (cm)	Domain length (cm)	U_o (cm/s)	T (s)
E05	(2) slightly merged sinusoidal ripples	1.4	12.0	8.0	12.0	40.0	2.0
E08	(1) sinusoidal ripple	0.8	24.0	8.0	24.0	40.0	2.0
E10	(2) sinusoidal ripples	1.6	12.0	8.0	12.0	40.0	2.0
E09	(3) sinusoidal ripples	1.6	24.0	12.0	24.0	40.0	2.0
E18	flat bed	0.0	0.0	4.0	8.0	20.0	1.0

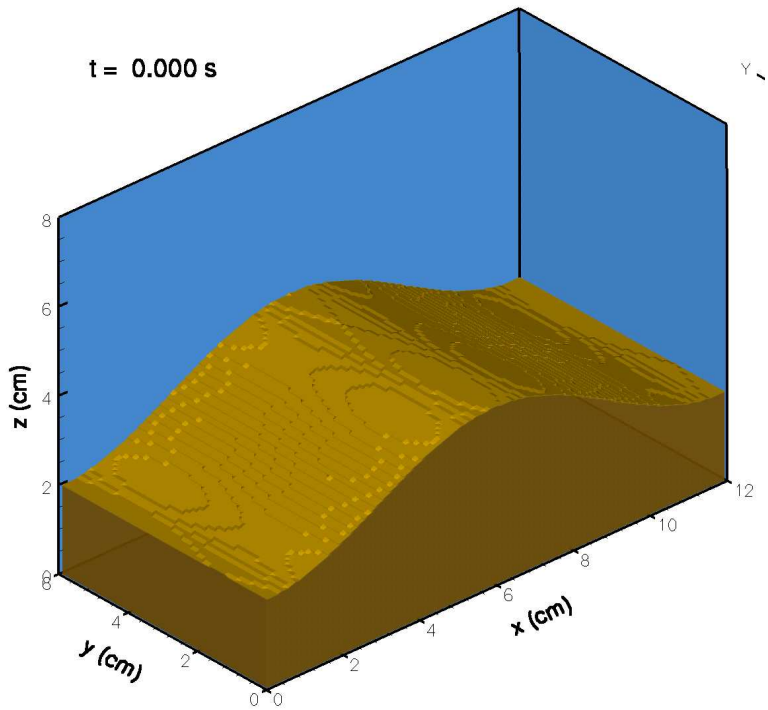

Figure 3–2. Initial bed state of the three-dimensional ripple amplitude simulation. A three-dimensional 2 cm ripple is initialized in a 12 cm x 6 cm x 8 cm domain.

Table 3–4. Model simulation parameters and laboratory data results. The free-stream velocity, wave period, and the grain size diameter are inputs to the model. Equations 1–2 and 1–1 describe the particle excursion and the mobility number, respectively. The predicted ripple height and length are from Nielsen's formulas (Equations 3–1 and 3–3).

Free-stream velocity U_o (cm/s)	Wave period T (s)	Grain size d (cm)	Particle excursion A (cm)	Mobility number ψ	Predicted ripple length λ (cm)	Predicted ripple height η (cm)
20.0	1.0	0.04	3.2	6.2	4.0	0.7
20.0	2.0	0.04	6.4	6.2	7.9	1.4
40.0	2.0	0.04	12.7	24.7	12.6	2.1
60.0	2.0	0.04	19.1	55.6	15.5	2.1
120.0	4.0	0.04	76.4	222.5	N/A	N/A

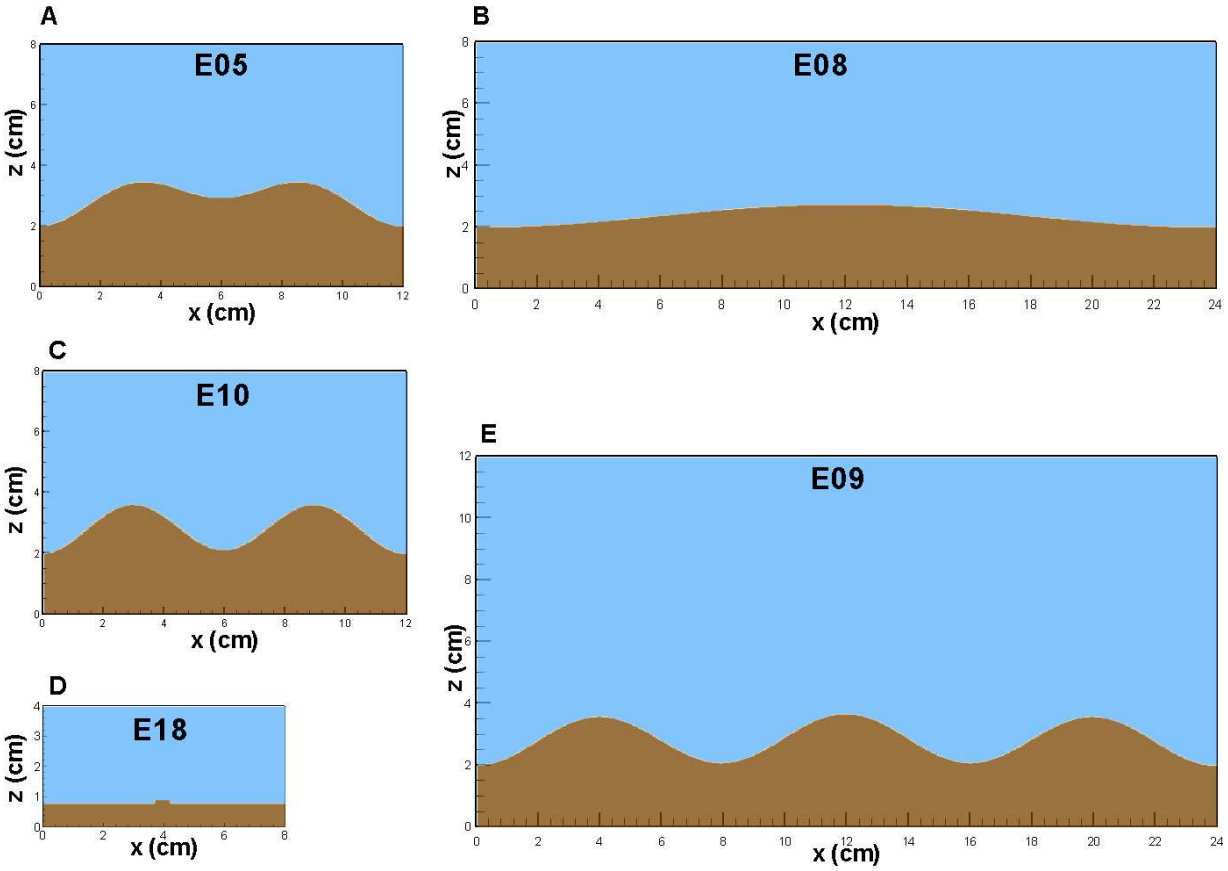

Figure 3–3. Initial bed states of the ripple wavelength simulations. (a) Case E05, (b) case E08, (c) case E10, (d) case E18, and (e) case E09.

CHAPTER 4
RESULTS

Twelve model simulations are presented in this work. From the simulations, we found that the model produces results similar to nature. The model has been tested for flows with Reynolds numbers from 10^4 to 10^5 and is found to predict ripple size and shape reasonably well under the tested conditions. For higher Reynolds numbers above the ripple producing regime, the model correctly produces no ripples.

The cases simulated for this work can be split into three groups. The ripple amplitude simulations examine the effect on ripple height evolution from the initiation of different ripple heights. The ripple amplitude flow velocity simulations show the ripple change due to varying free-stream velocities. The two ripple and three ripple wavelength simulations illustrate how a ripple length and height adjusts towards equilibrium over time. A flatbed case and a three-dimensional case are also presented in this chapter.

4.1 Ripple Amplitude Simulations

The first three cases presented have the same flow conditions and sediment properties (see Table 3–1 for details). The simulations illustrate the evolving ripple height and shape. Figure 4–1 shows snapshots in time of the ripple evolution throughout the simulations.

4.1.1 Ripple Height

The top four panels of Figure 4–1 show the progression of the ripple in case E03. The simulation is initialized with a bedform 1 cm in height and 12 cm in length. Through the 16 second simulation, the initial 1 cm ripple grows to 1.5 cm. The ripple in case DC05 (Figure 4–1(b)) is initialized at 2 cm and decays 0.5 cm to a height of 1.5 cm after 16 seconds. In case E04 (Figure 4–1(c)), the initial 3 cm ripple decays to a 1.5 cm ripple. Figure 4–2 is a plot of the evolution of maximum ripple height (η_{max}) for the three cases. The maximum ripple height is the distance between the minimum point in the ripple trough and the maximum height of the ripple crest. The ripples in the three simulations equilibrate to 1.5 cm after being initialized at different heights. According to

Nielsen's formula, the equilibrium ripple height for the given flow conditions is 2 cm (η_e in Figure 4–2). Computational constraints made it expensive to conduct the simulations for longer than 16 seconds, but continuing the simulation further was deemed unnecessary since the three simulations achieved the same balanced condition by this time.

4.1.2 Ripple Shape

This set of simulations is initialized with a sinusoidal ripple, a shape not realistically seen in nature. Throughout the simulations, the ripples in each of the cases presented evolve to a more peaked, pointed, and steeper shape than the initialized sinusoid. Figure 4–3 illustrates this concept for case E03 (Figure 4–3(a)), DC05 (Figure 4–3(b)), and E04 (Figure 4–3(c)). The top three panels of Figure 4–3 show the ripple isosurface, ζ_x, at $t = 0$ seconds and $t = 16$ seconds for the three cases. The isosurface of the ripple is determined as the height above the bottom of the domain when the volumetric concentration drops below 50% (Equation 4–1). Initially, the ripples have mildly sloping sides and rounded peaks. As the simulation progresses, the ripples become more peaked.

$$\text{ripple isosurface}_x = \zeta_{x_{|c=0.5}} \tag{4–1}$$

To quantify the side slopes of the ripple, the derivative of the ripple isosurface height is taken and averaged over eight grid points. That quantity is then normalized with the maximum height of the ripple at the current time, $\eta_{max,t}$ (Equation 4–2). The middle three panels of Figure 4–3 show the eight grid point averaged slope over the length of the ripple at the initial and final times. At $t = 0$ seconds, the slope is smooth and gradual. At $t = 16$ seconds, the distance between the maximum and minimum slope is smaller than the distance in the initial profile, indicating a much less gradual slope and more peaked apex.

$$\text{ripple slope}_x = \frac{d\left(\zeta_{x_{|c=0.5}}\right)}{dx} * \frac{1}{\eta_{max,t}} \tag{4–2}$$

The increased peakedness is also illustrated in the bottom three panels of Figure 4–3. The slope change over the length of the ripple (Equation 4–3) is plotted in these graphs. The initial profile slope change is relatively small compared to the slope change of the final profile. At $t = 16$ seconds, the slope change is greater at the center of the ripple, indicating an increase in peakedness from the initial profiles. Also in the simulation, the ripple peak sways side to side, similar to what is seen in nature.

$$\text{ripple slope change}_x = \frac{d}{dx}\left(\frac{d\left(\zeta_{x_{|c=0.5}}\right)}{dx} * \frac{1}{\eta_{max,t}}\right) \tag{4–3}$$

4.1.3 Suspended and Bed Load Transport

Details of the modes of ripple growth and decay are currently unknown. The specific driving mechanism of ripple morphology (i.e., bed load transport, suspended load transport, or a combination of both) is difficult to measure in the laboratory and field, and a live-bed, sediment transport model capable of closely examining sand ripple dynamics has not previously existed. From our model, we are able to calculate the bed and suspended load fluxes that cause the sand ripple to evolve. In this study, bed load is defined to be within $4.6d$ of the stationary bed. Figure 4–4 shows a time series of the calculated time-dependent, vertically-, and horizontally-averaged load transport fluxes (see Appendix A for an explanation of the calculations). When the flux is negative, it is contributing to ripple amplitude decay. A positive flux contributes to the growth of the ripple amplitude. Plots (a), (b), and (c) are the instantaneous bed and suspended load fluxes for cases E03, DC05, and E04, respectively. Plots (d), (e), and (f) are the cumulative sum of the bed and suspended load fluxes for cases E03, DC05, and E04, respectively. As shown previously, case E03 has a growing ripple, case DC05 has a slightly decaying ripple, and case E04 has a more rapidly decaying ripple. In the case of the growing ripple (E03), the suspended load fluxes are almost zero and the bed load fluxes are positive and dominate the ripple change (Figure 4–4(a) and 4–4(d)). Therefore, the

bed load transport is the main contributor to ripple growth. For the rapidly decaying ripple case (E04), the bed load flux is negative and therefore, bed load sediment transport is also the cause of a decrease in ripple height (Figure 4–4(f)). Figure 4–4(e) shows the fluxes for the weakly decaying ripple case. Again, the bed load fluxes are negative and are the cause of the slight decay. However, both bed and suspended load fluxes are small in comparison to the other cases.

Similar to the field and laboratory, there is also imprecision in the divisions of bed and suspended load when analyzing the model results. For example, the suspended load that has not yet settled out of the water column is counted as contributing to ripple growth in the analysis. This idea is illustrated in the rapidly decaying case, E04. In this simulation, the suspended load fluxes are large and seem to contribute to ripple growth. These high suspended load fluxes are due to the tall height of the ripple in case E04. The simulation is initialized with a ripple having a height of 3 cm. The ripple is exposed to more of the force of the flow than the other two cases. The boundary layer becomes large and a more turbulent flow erupts around the ripple. This turbulence causes more vortices to shed off the lee sides of the ripple and therefore causes more suspended sediment. These suspended sediment fluxes are counted in the growth and decay flux calculations, even though they are still in the water column and not affecting the ripple. Additionally, a slight slumping of the underlying bed material was sometimes observed. Finally, the results are somewhat sensitive to the precise definition of the concentration threshold chosen to define bed load and suspended load (see Appendix A for details).

4.1.4 Advective, Settling, and Diffusive Fluxes

This section concentrates on the type of fluxes that cause ripple evolution. (refer to Appendix A for a detailed explanation of the fluxes). There are three types of fluxes that can move sediment. Advective fluxes are due to the flow caused by the wave oscillations in the water column. The ripple causes a disturbance in the flow, which in turn creates vortices that pick up and move sediment. A second form of sediment movement is

by diffusive flux. Diffusion is a natural tendency for the components of a mixture to move from a region of high concentration to a region of low concentration. Mass can be transferred by random molecular motion in quiescent fluids, or it can be transferred from a surface into a moving fluid, aided by the dynamic characteristics of the flow. Settling is the third type of flux. This motion is purely due to gravity causing the settling of the sediment. Figure 4–5 shows the instantaneous and cumulative averaged diffusive, advective, and settling fluxes for case E03, DC05, and E04. The negative settling fluxes indicate ripple decay. Therefore, one cause of a decrease in ripple height is grains sliding from the peak down the sides of the ripple and settling in the trough. The opposite occurs for the diffusive fluxes. The sediment layer above the immobile bed thickens at the crest and thins in the trough, possibly because of the shearing off of the peak from the flow and the settling of grains into the trough. This diffusive flux is a cause of ripple growth. The settling and diffusive fluxes are nearly equally balanced and have a non-zero value even with no flow. This balance is apparent in the sediment continuity governing equation (Equation 2–9) as gravitational settling is counteracted by an upward diffusion across the thin concentration gradient at the ripple surface and in the core of the sediment suspension plumes. Therefore, the average of these fluxes could be subtracted out, leaving the advective fluxes as the primary cause of the sediment transport. Figure 4–6 shows the three types of fluxes averaged in time, the x-, and, the y-directions for case E03, DC05, and E04. Included on the plots are the initial and final (at t=0 seconds and t=16 seconds, respectively) ripple crest and trough heights. The figure also shows the balance between the settling and diffusive fluxes. The growing ripple case (Figure 4–6(a)) demonstrates a slightly larger positive diffusive flux than settling flux and yields positive advective fluxes at the crest and trough, leading to ripple growth. Both the diffusive and settling fluxes in the slightly decaying ripple case (Figure 4–6(b)) are well balanced. The advective fluxes are slightly negative, agreeing with the small decrease in the ripple amplitude. The diffusive and settling fluxes are also balanced in the rapidly decaying case (Figure 4–6(c)).

The negative advective fluxes cause the decrease of the crest height and the slightly more negative diffusive fluxes produce the increased trough height.

4.2 Ripple Amplitude Flow Velocity Simulations

The following three simulations are initialized with the same oscillation period and similar initial ripple heights but with different oscillatory flow velocities. A low energy case (E11) is initialized with a 2.2 cm sinusoidal ripple and forced with a 20 cm/s maximum free-stream velocity flow. Case E13, a mid-energy simulation, has a 60 cm/s maximum free-stream velocity and a 2 second period. The high energy case, E20, is forced with an oscillatory flow with 120 cm/s maximum free-stream velocity. The ripple is expected to shear off under this strong flow, evolving from the initial 1.6 cm ripple amplitude to no stable ripple form. Figure 4–7 illustrates a time series of ripple evolutions for the three cases. Table 3–1 includes detailed conditions of the simulations.

4.2.1 Ripple Height

The ripple height evolution ($\eta_{max,t}$) and expected equilibrium ripple height (η_e) for all three cases can be seen in Figure 4–8. The low energy case (E11) is shown in panels 4–7(a). Under the flow conditions, a 1.4 cm ripple height is expected to develop in equilibrium. Over the 20 second simulation, the ripple decays from 2.2 cm to 0.8 cm, as shown in Figure 4–8(a). It can be deduced from the results that the ripple is not yet in equilibrium. For the mid energy case, E13, the initial 1.6 cm ripple should grow to about 2.1 cm. Figure 4–7(b) shows the ripple grows from 1.6 cm in height to 2 cm in height in three wave periods. The growth is steady throughout the simulation. In the high energy case, E20, the ripple decays from a 1.6 cm ripple to a rough bed with no definite or stable ripple shape.

4.2.2 Suspended and Bed Load Transport

Figure 4–9 shows the suspended and bed load fluxes for the low, mid, and high energy cases. Panels (a), (b), and (c) are the instantaneous fluxes and panels (d), (e), and (f) are the cumulative sum of the fluxes for the three cases. The low flow case, E11

(Figure 4–9(a) and (d)), has essentially no suspended sediment and illustrates that the decline in ripple height occurs due to bed load sediment transport. At this point in the simulation, the height is 0.6 cm less than the equilibrium ripple height as determined by Nielsen's steady-state formula. As previously mentioned, this difference is most likely due to the ripple not yet being in its equilibrium state. Figure 4–9(d) supports this hypothesis. The bed load fluxes in the end of the simulation are increasing, now contributing to ripple growth. Time constraints prevented running the simulation further. Future research will examine a longer simulation. The ripple in case E13 (Figure 4–9(e)) grows 0.4 cm mostly through bed load sediment transport. Some suspended sediment transport decreases the ripple height, but not enough to overcome the growth due to bed load transport. In the high energy case, E20, there are equal but opposite amounts of bed and suspended load transport, but bed load transport causes the ripple decay. The large amount of positive suspended sediment flux is due to the high energy of the flow, and may not necessarily induce ripple growth.

4.3 Two Ripple Wavelength Simulations

The remainder of the simulations presented in this work (excluding the three-dimensional case) examine both ripple height and wavelength evolution. Cases E05 and E10, shown in Figure 4–10, are forced with the same oscillatory flow, but have different initial ripple shapes. Case E05 (Figure 4–10(a)) is initialized with two slightly merged ripples, creating a "double-crested" ripple that is 1.4 cm in height and 12 cm in length. Two separate ripples are initialized in case E10 (Figure 4–10(b)), again with a total length of 12 cm. Refer to Table 3–3 for other conditions of the simulations.

4.3.1 Ripple Wavelength

Initializing the model with multiple ripples in a domain allows more for the evolution of ripple length in addition to ripple height. In the one ripple cases, the ability for the length to change is limited by the domain because the ripple is initialized at its expected equilibrium length for the given flow conditions. In these two cases, two ripples

are initialized in a 12 cm domain, which is the equilibrium length of just one ripple for the simulation flow characteristics according to Nielsen's formula. In case E05, the peaks of the "double-crested" ripple merge to form one ripple with a length of 12 cm (Figure 4–10(a)). Case E10 is initialized with two ripples, each 6 cm in length. The two ripples slowly merge throughout the 65 second simulation to a shape that resembles the beginning stages of case E05. This similarity to the previous case whose ripples eventually did merge together to form one ripple suggests that case E10 will follow the results of case E05 if the simulation was run longer than 65 seconds. Again, time constraints led to the investigation of other questions rather than attempting to confirm this detail.

4.3.2 Ripple Height

Figure 4–11 plots the maximum ripple height evolution for the "double-crested" (E05) and two-ripple (E10) cases. The height of the "double-crested" ripple to the merged single ripple decreases from 1.4 cm to 1 cm. The initial decrease is steep, but then the ripple height steadies and slowly rises, indicating the ripple should continue to grow past the 30 second simulation. In the two-ripple case (E10), the ripple height decreases fairly quickly, then steadies as the peaks of the two ripples slowly merge. Similar to the ripple wavelength comparison, the final ripple height in case E10 is about the same as the 16 second panel of case E05. Past 65 seconds, the ripple in this simulation is expected to start to slowly rise, just as the ripple does in case E05. Both of the simulations were terminated due to time constraints and could be examined more in the future.

4.3.3 Suspended and Bed Load Transport

Figures 4–12(a) and 4–12(c) show the instantaneous and cumulative fluxes, respectively, for the "double-crested" ripple case (E05). The suspended load transport is minimal and it seems that the bed load transport causes a slight decay then growth of the ripple. In the two-ripple cumulative flux plot (Figure 4–12(d)), the positive bed load fluxes indicate that the bed load transport should be causing ripple growth, not decay. The flux plot for this case contradicts the results from all the previous cases. The

discrepancy could be due to the movement of the peaks of the ripples and the merging of the two ripples into one that causes positive bed load fluxes even though the ripple is not growing (see Appendix A).

4.4 One and Three Ripple Wavelength Simulations

The next two cases presented also examine ripple height and length evolution, but in a domain where two ripples are expected to develop in equilibrium. Both are forced with oscillatory flows with a 40 cm/s maximum free-stream velocity and 2 second period. Figures 4–13(a) and 4–13(b) are simulation frames from case E08 and E09, respectively. Case E08 is initialized with one ripple 24 cm in length and 0.8 cm in height. Three ripples, each 8 cm in length and 1.6 cm in height, are initialized in case E09.

4.4.1 Ripple Wavelength

The one-ripple case (E08) has a domain length of 24 cm, which is the length of two equilibrium ripples. As the 41 second simulation progresses, four small ripples, each about 6 cm in length, form and begin to grow. Although we expect there to be only two ripples in the domain at equilibrium, research has shown (Grant and Madsen, 1982; O'Donoghue and Clubb, 2001) that ripples about half the equilibrium size form first on an almost flat bed, before reaching a final equilibrium state. It is also interesting that the initial long ripple still somewhat exists and that the small ripples have formed on its surface. This is also seen in laboratory experiments. It is necessary for the simulation to be run further before confirming the model agrees with previous findings on ripple evolution. The same size domain is used in the three-ripple case (E09). After the 40 second simulation, the wavelengths of the three ripples are unchanged, but the ripples are less defined. As with the one-ripple case, the simulation would need to be run longer for further examination.

4.4.2 Ripple Height

Figure 4–14 shows the ripple height evolution for the one- and three-ripple cases. In case E08, four small ripples form on the long flat ripple. They grow from about 0.8 cm to 1 cm and are still growing at the end of the simulation (Figure 4–14(a)). The

ripples are not steady and their crests sway back and forth. The ripples on the far left and right are smaller and less defined than the two middle ripples (Figure 4–13(a)). Along with the changing ripple height, this evidence supports that the simulation is not yet in its equilibrium state. The three ripples in case E09 decay from 1.6 cm to 0.7 cm in the 40 second simulation (Figure 4–14(b)). The left ripple becomes less defined than the other two ripples, which suggests the three ripples might merge into two past 41 seconds (Figure 4–13(b)). Again, this case would need to be run longer in order to confirm this hypothesis.

4.4.3 Suspended and Bed Load Transport

The suspended and bed load fluxes for cases E08 and E09 are shown in Figure 4–15. The cumulative flux plot for the one-ripple case (Figure 4–15(c)) indicates that the suspended load fluxes are small compared to the bed load fluxes. Therefore, bed load transport is the main cause of ripple growth and shape change. This observation is also apparent in the simulation frames where it can be seen that there is very little suspended sediment present throughout the simulation. Similar to the two-ripple case (E10), the flux plot for the three-ripple case (Figure 4–15(d)) is contradictory to the other cases. The large positive increase of bed load flux indicates the ripples should be growing due to bed load sediment transport. See Section 4.3.3 and Appendix A for further explanation.

4.5 Flatbed Simulation

The final two-dimensional case presented examines the ripple evolution from a flat bed with just a small perturbation. The 41 second simulation is forced with an oscillatory flow with a 20 cm/s maximum free-stream velocity and a 1 second period. Figure 4–16 shows the time series evolution of the simulation. The domain has a length of 8 cm, twice the length of the expected equilibrium ripple for the flow conditions.

4.5.1 Ripple Height

The time series of ripple evolution for the flatbed case is shown in Figure 4–17. Within 10 seconds of the simulation, one small ripple forms in the center of the domain.

Ripples soon start to form on either side of the center ripple. After 41 seconds, three defined ripples are present in the domain. The expected equilibrium ripple height for the current flow conditions is 0.7 cm (η_e on Figure 4–17). The ripples grow from the flat bed to about a height of 0.3 cm. From previous research (mentioned in Section 4.4.1), ripples formed from a flat bed start as small rolling grain ripples and develop into larger vortex ripples after many flow periods $O(10^2)$. Further examination of this case is necessary to determine whether the ripples will evolve into their equilibrium state.

4.5.2 Ripple Wavelength

The expected equilibrium ripple wavelength for this case is 4 cm, half as large as the domain. Three ripples, each about 2.7 cm in length, have formed inside the domain after the 41 second simulation. The previous simulations have examined the results of forcing a flow over an existing ripple. This case shows the model's ability to predict the formation of ripples from an almost completely flat bed.

4.5.3 Suspended and Bed load Transport

The instantaneous and cumulative load fluxes are shown in Figures 4–18(a) and 4–18(b), respectively. As seen in the simulation snapshots, there is no suspended sediment in the simulation. These ripples are still rolling-grain ripples; no vortices are formed and therefore, no sediment gets suspended. The ripples are made purely from bed load sediment transport.

4.6 Three-Dimensional Simulation

One fully three-dimensional simulation (out of three that were examined with different domain sizes) is presented here. This is due to the large amount of computational time necessary for a three-dimensional simulation. Advances in technology and a reorganization of the numerical code could shorten the computational time required. Further research will concentrate more on three-dimensional simulations.

Case E14 has a domain of 12 cm by 6 cm by 8 cm and is forced with an oscillatory flow (maximum free-stream velocity of 40 cm/s) with a 2 second period. The simulation is

initialized with a ripple 2 cm in height and 12 cm in length. Its initial conditions and flow characteristics are the same as the quasi-two-dimensional slightly decaying case (DC05). As with case DC05, only the evolution of the ripple height is examined.

4.6.1 Ripple Height

Figure 4–20 shows the ripple height evolution throughout the simulation. The ripple is initialized with a height of 2 cm, the same steady-state ripple height according to Nielsen's formula. Instead of the ripple height decreasing 0.5 cm like the two-dimensional slightly decaying case, it stays steady at the equilibrium ripple height of 2 cm. The differences between the quasi-two- and three-dimensional cases will be discussed in Chapter 5.

4.6.2 Suspended and Bed Load Transport

The suspended and bed load fluxes, shown in Figure 4–21, are nearly equal and opposite in sign. The suspended load fluxes are positive, contributing to sand ripple growth. The bed load fluxes are equally negative, causing ripple decay. The equal and opposite transport mechanisms create a dynamic equilibrium with the ripple height relatively steady and unchanging. Note that the change of the ripple shape from a sinusoid to a more peaked and steep shape requires a small net flux.

4.7 Summary of Results

All of the cases presented in this work show the potential of this model to advance the understanding of sand ripples and sediment transport. Tables 4–1 and 4–2 summarize the results. The conclusions and discussion of these results are presented in Chapter 5.

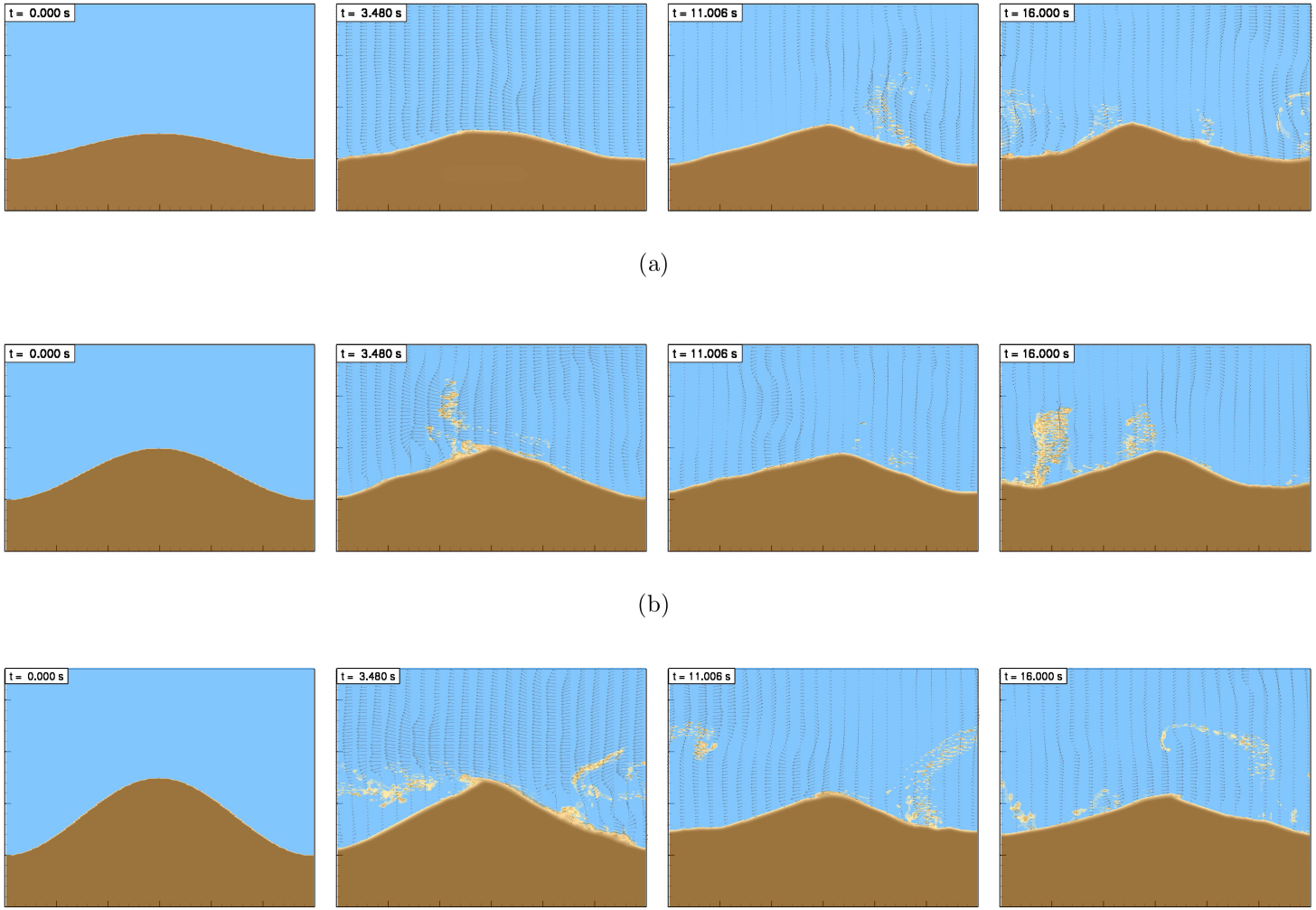

Figure 4–1. Snapshots in time of the ripple amplitude simulations. (a) growing ripple case (E03) with $U_o = 40$ cm/s, $T = 2$ s, and $\eta_o = 1$ cm. (b) Slightly decaying ripple case (DC05) with $U_o = 40$ cm/s, $T = 2$ s, $\eta_o = 2$ cm. (c) Rapidly decaying ripple case (E04) with $U_o = 40$ cm/s, $T = 2$ s, $\eta_o = 3$ cm.

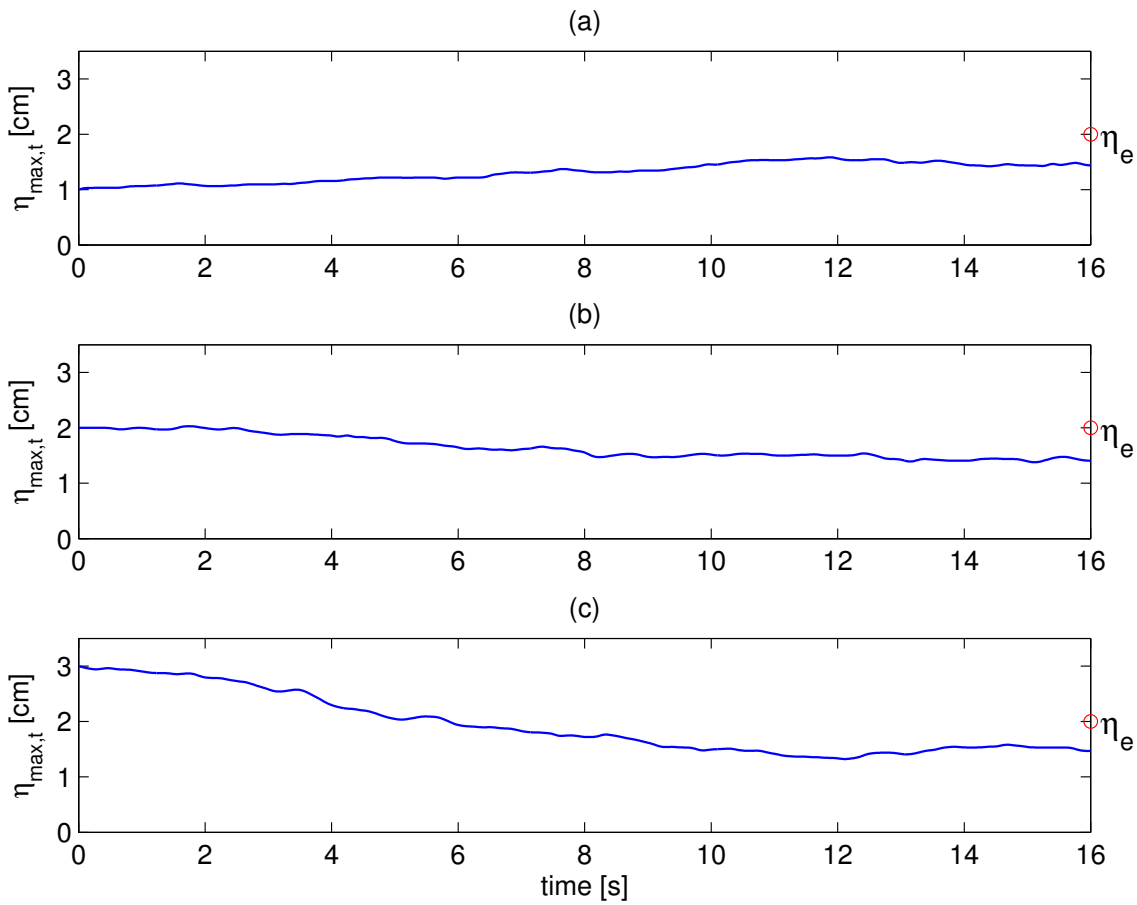

Figure 4–2. Time evolution of the maximum ripple height ($\eta_{max,t}$) for the (a) growing ripple case (E03), (b) slightly decaying ripple case (DC05), and (c) rapidly decaying ripple case (E04). η_e denotes the equilibrium height resulting from Nielsen's steady-state formulas for the simulation conditions.

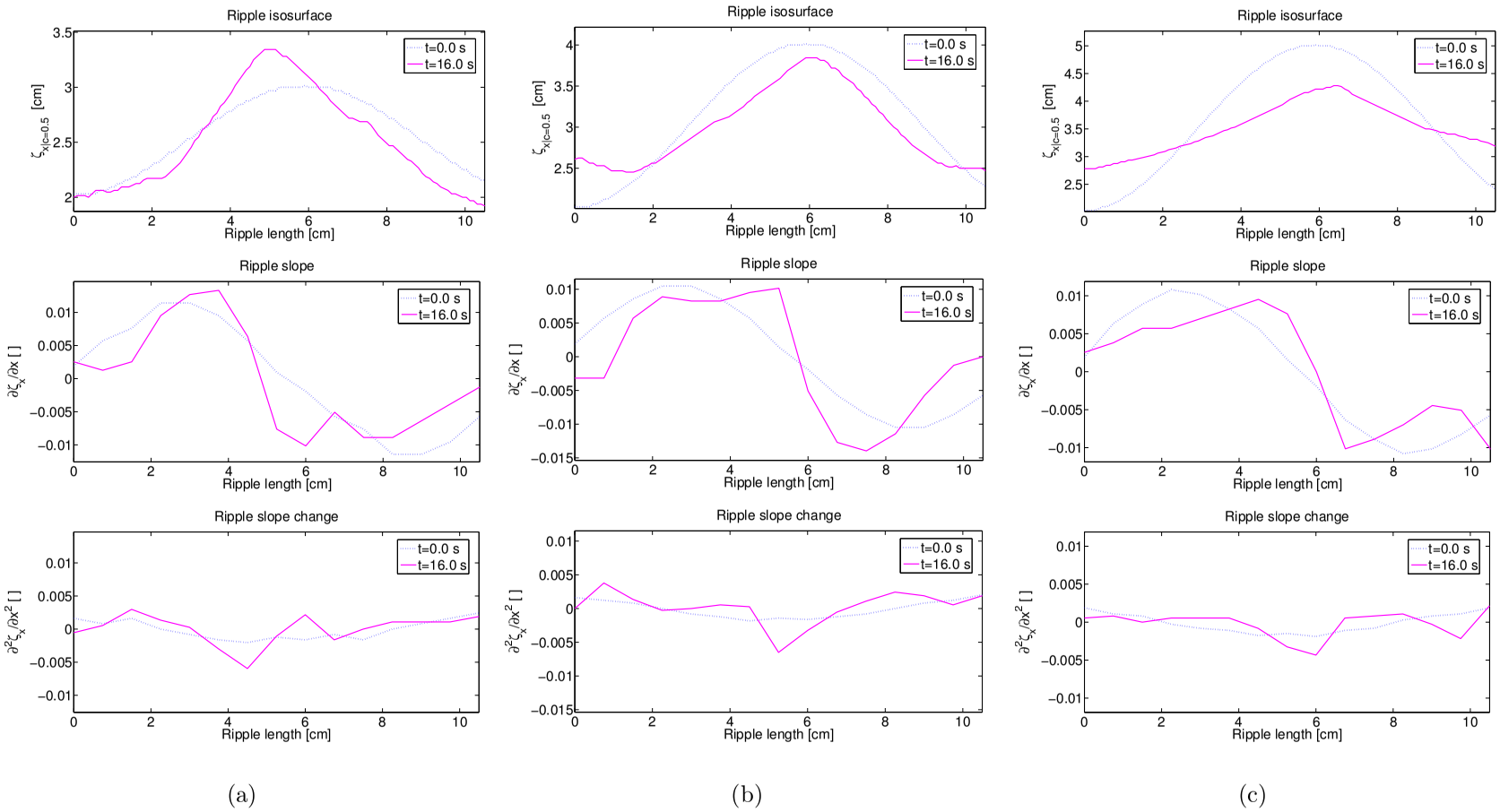

Figure 4–3. Plots of the initial and final ripple isosurface, slope, and slope change for the (a) growing ripple case (E03), (b) slightly decaying ripple case (DC05), and (c) rapidly decaying ripple case (E04).

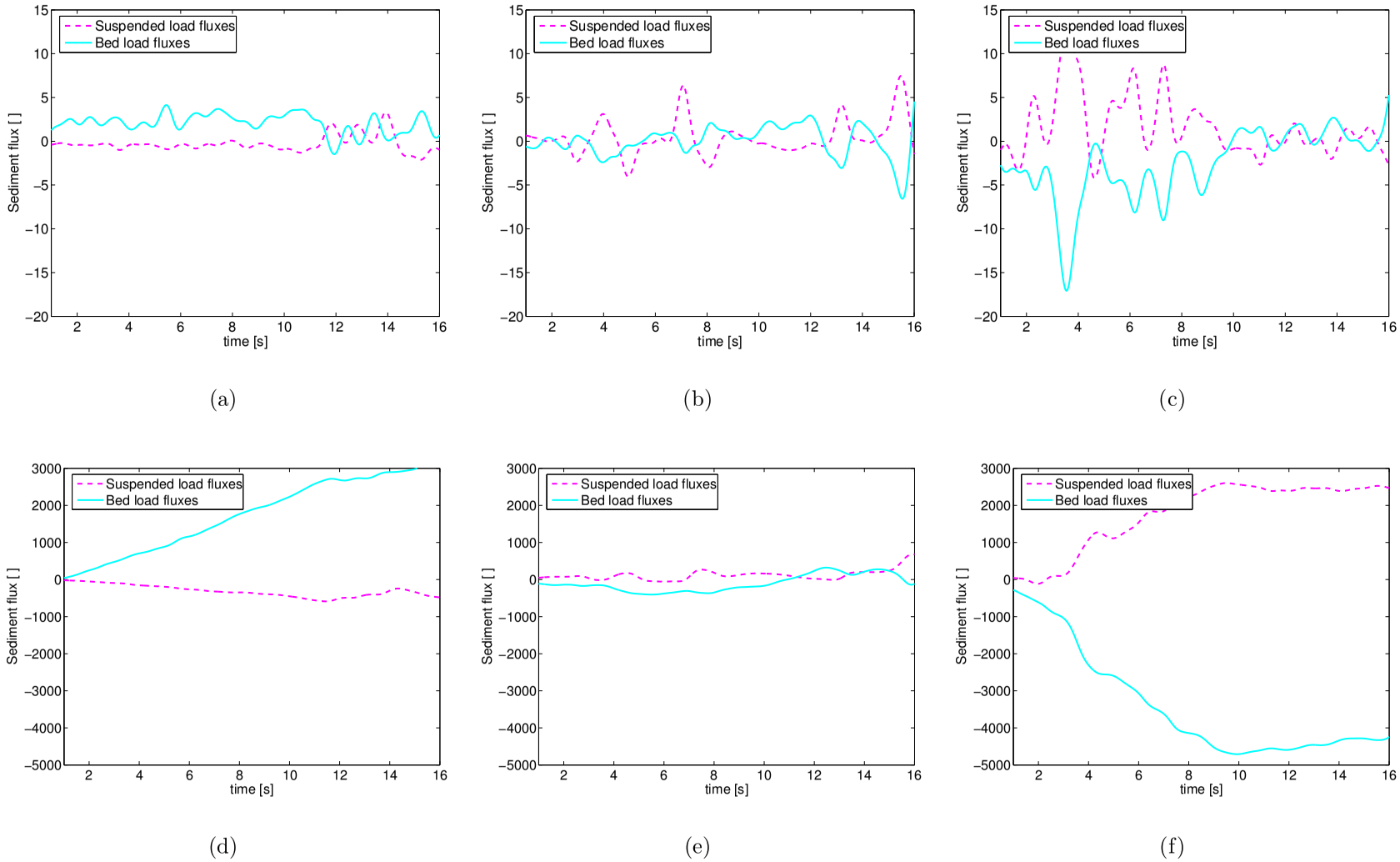

Figure 4–4. Instantaneous averaged bed and suspended load fluxes for the (a) growing (E03), (b) slightly decaying (DC05), and (c) rapidly decaying (E04) cases. Cumulative averaged bed and suspended load fluxes for the (d) growing (E03), (e) slightly decaying (DC05), and (f) rapidly decaying (E04) cases.

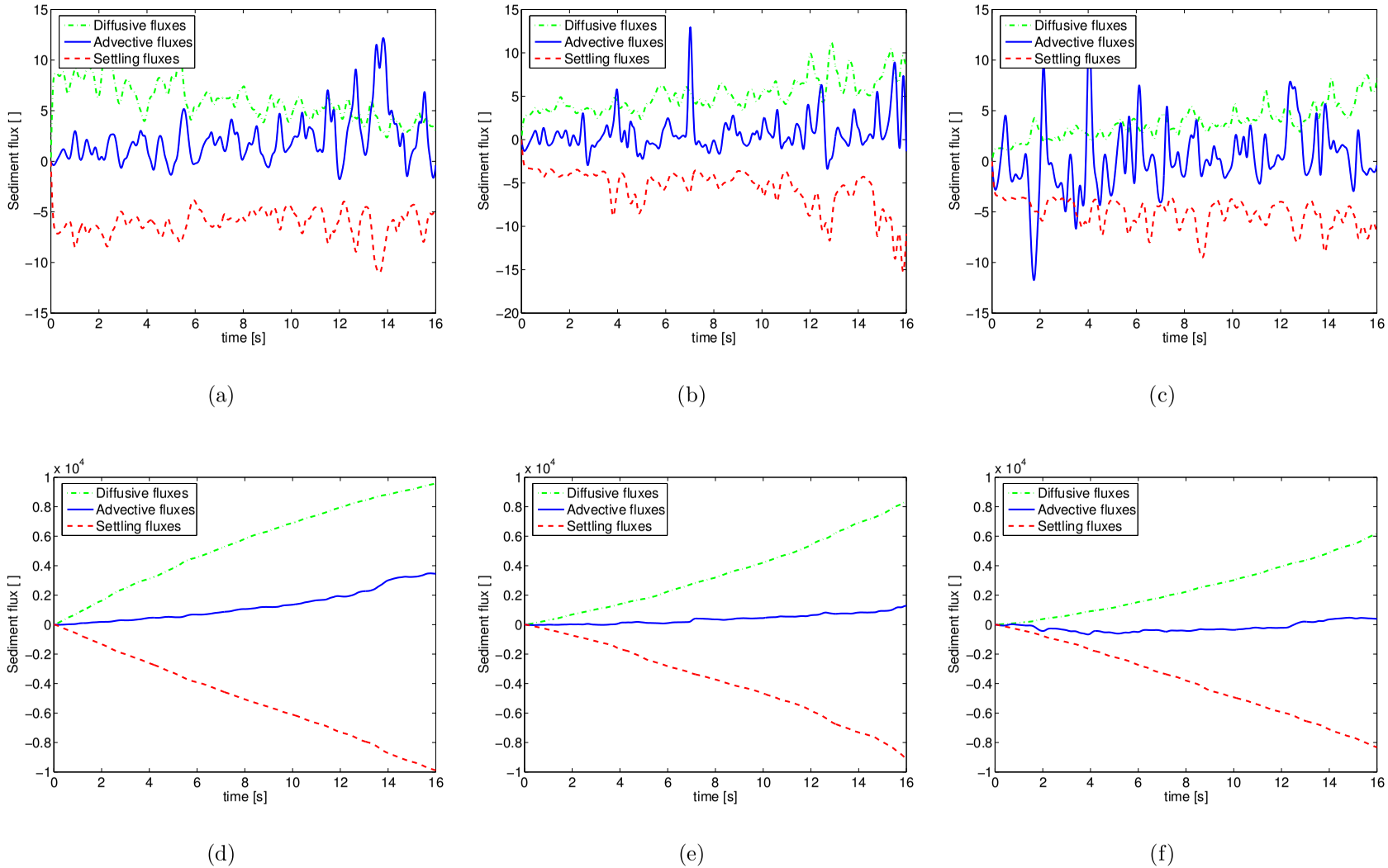

Figure 4–5. Instantaneous averaged advective, diffusive, and settling fluxes for the (a) growing (E03), (b) slightly decaying (DC05), and (c) rapidly decaying (E04) cases. Cumulative averaged advective, diffusion, and settling fluxes for the (d) growing (E03), (e) slightly decaying (DC05), and (f) rapidly decaying (E04) cases.

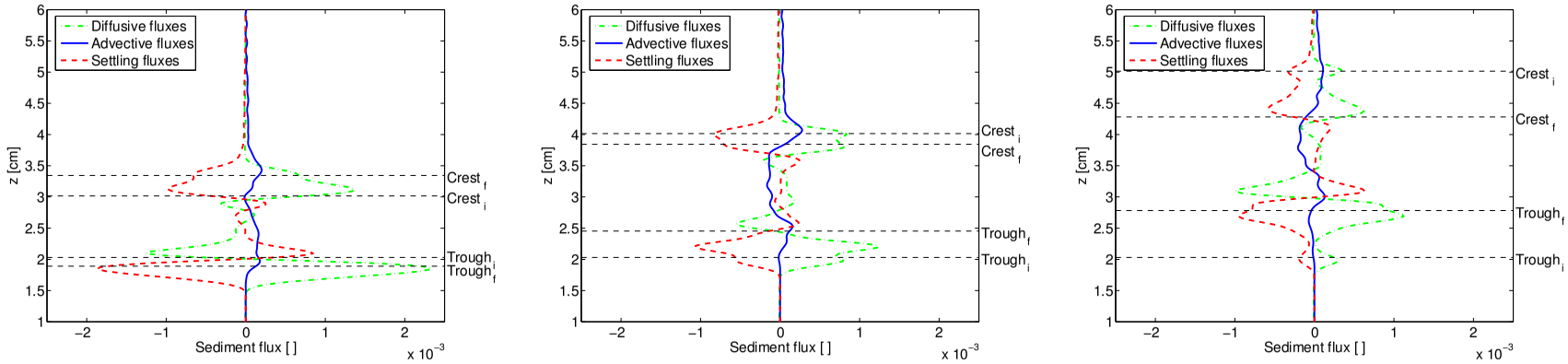

(a) (b) (c)

Figure 4–6. Time, x-, and y-averaged advective, diffusive, and settling flux plots for the (a) growing (E03), (b) slightly decaying (DC05), and (c) rapidly decaying (E04) cases.

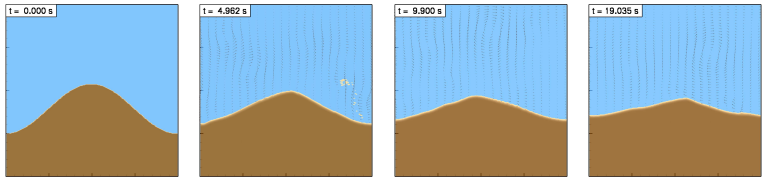

(a)

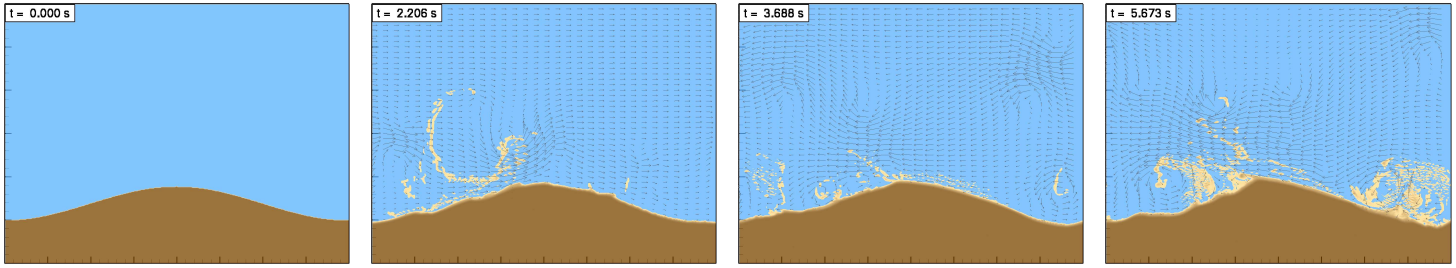

(b)

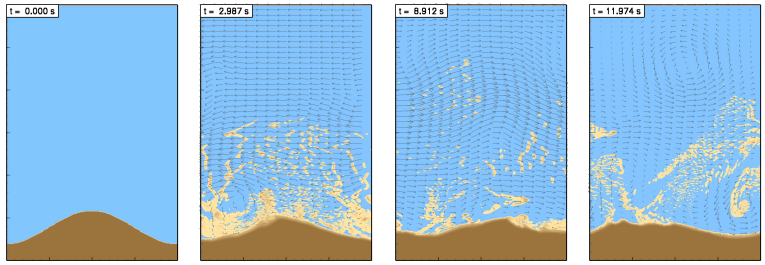

(c)

Figure 4–7. Snapshots in time of the ripple amplitude simulations with varying maximum free-stream velocities. (a) Low energy case (E11) with $U_o = 20$ cm/s, $T = 2$ s, $\eta_o = 2.2$ cm. (b) Mid-energy case (E13) with $U_o = 60$ cm/s, $T = 2$ s, $\eta_o = 1.6$ cm. (c) High energy case (E20) with $U_o = 120$ cm/s, $T = 4$ s, $\eta_o = 1.6$ cm.

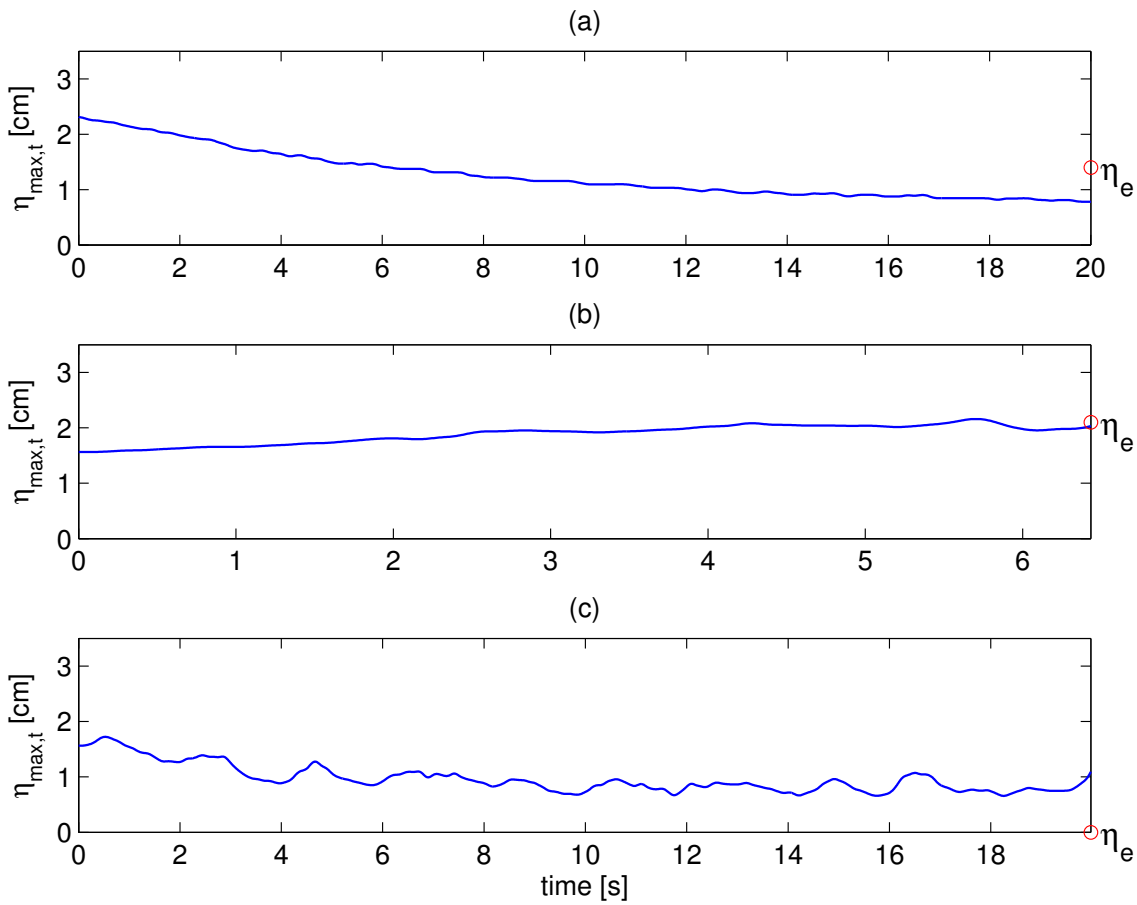

Figure 4–8. Time evolution of the maximum ripple height ($\eta_{max,t}$) for the (a) low energy case (E11), (b) mid-energy case (E13), and c) high energy case (E20). η_e denotes the equilibrium height resulting from Nielsen's steady-state formulas for the simulation conditions.

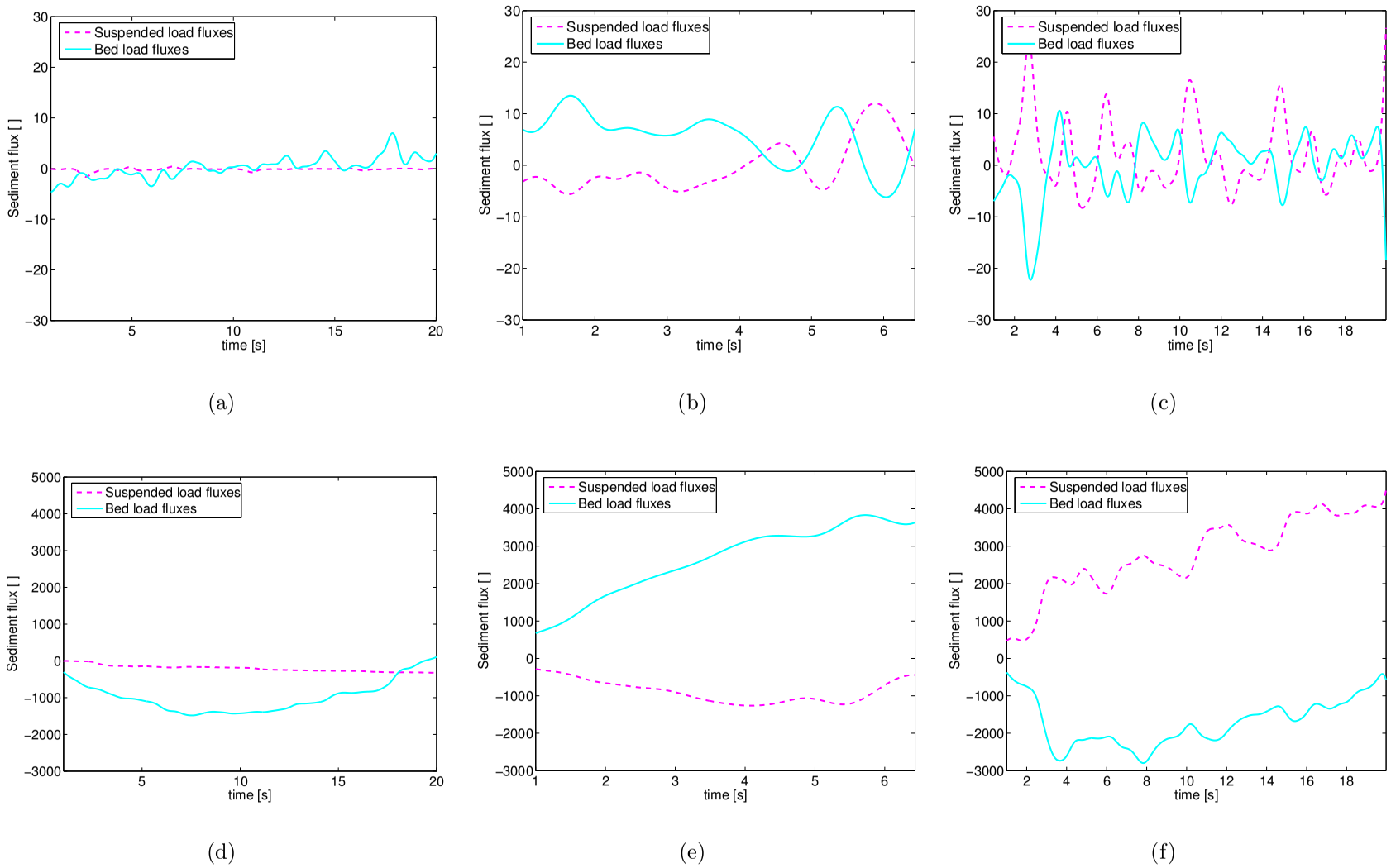

Figure 4–9. Instantaneous averaged bed and suspended load fluxes for the (a) low energy (E11), (b) mid energy (E13), and (c) high energy (E20) cases. Cumulative averaged bed and suspended load fluxes for the (d) low energy (E11), (e) mid energy (E13), and (f) high energy (E20) cases.

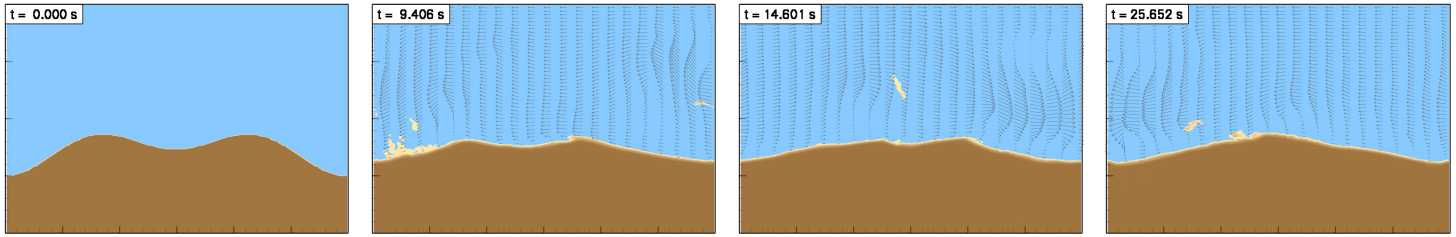

(a)

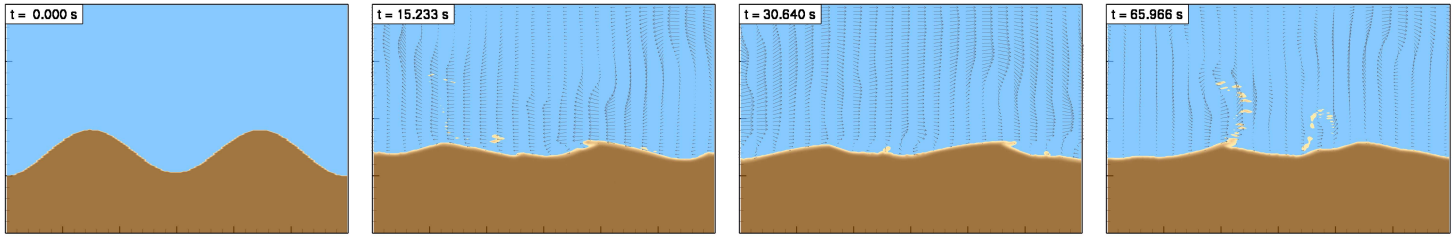

(b)

Figure 4–10. Snapshots in time of the two ripple wavelength simulations. (a) "Double-crested" ripple case (E05) with $U_o = 40$ cm/s, $T = 2$ s, $\eta_o = 1.4$ cm. (b) Two-ripple case (E10) with $U_o = 40$ cm/s, $T = 2$ s, $\eta_o = 1.6$ cm.

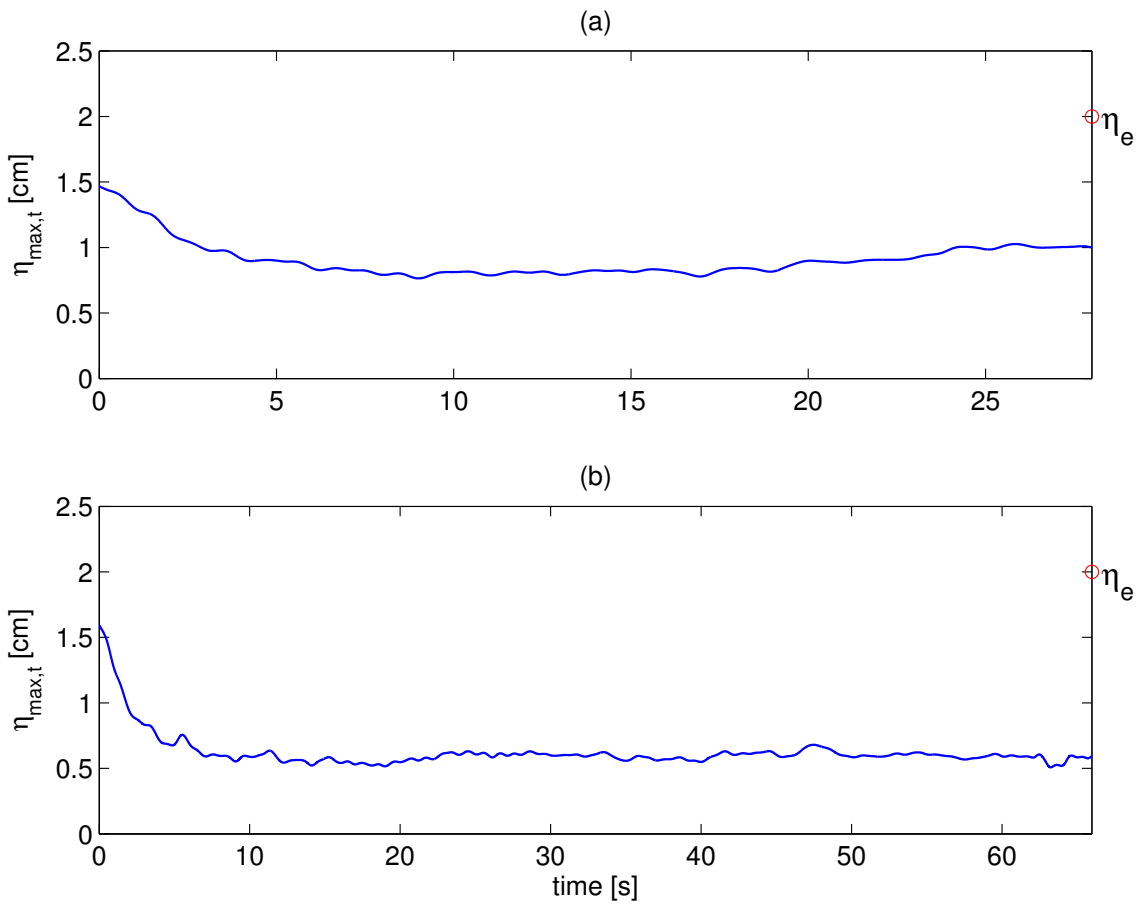

Figure 4–11. Time evolution of maximum ripple height ($\eta_{max,t}$) for the (a) "double-crested" ripple (E05), and (b) two-ripple (E10) cases. η_e denotes the equilibrium height resulting from Nielsen's steady-state formulas for the simulation conditions.

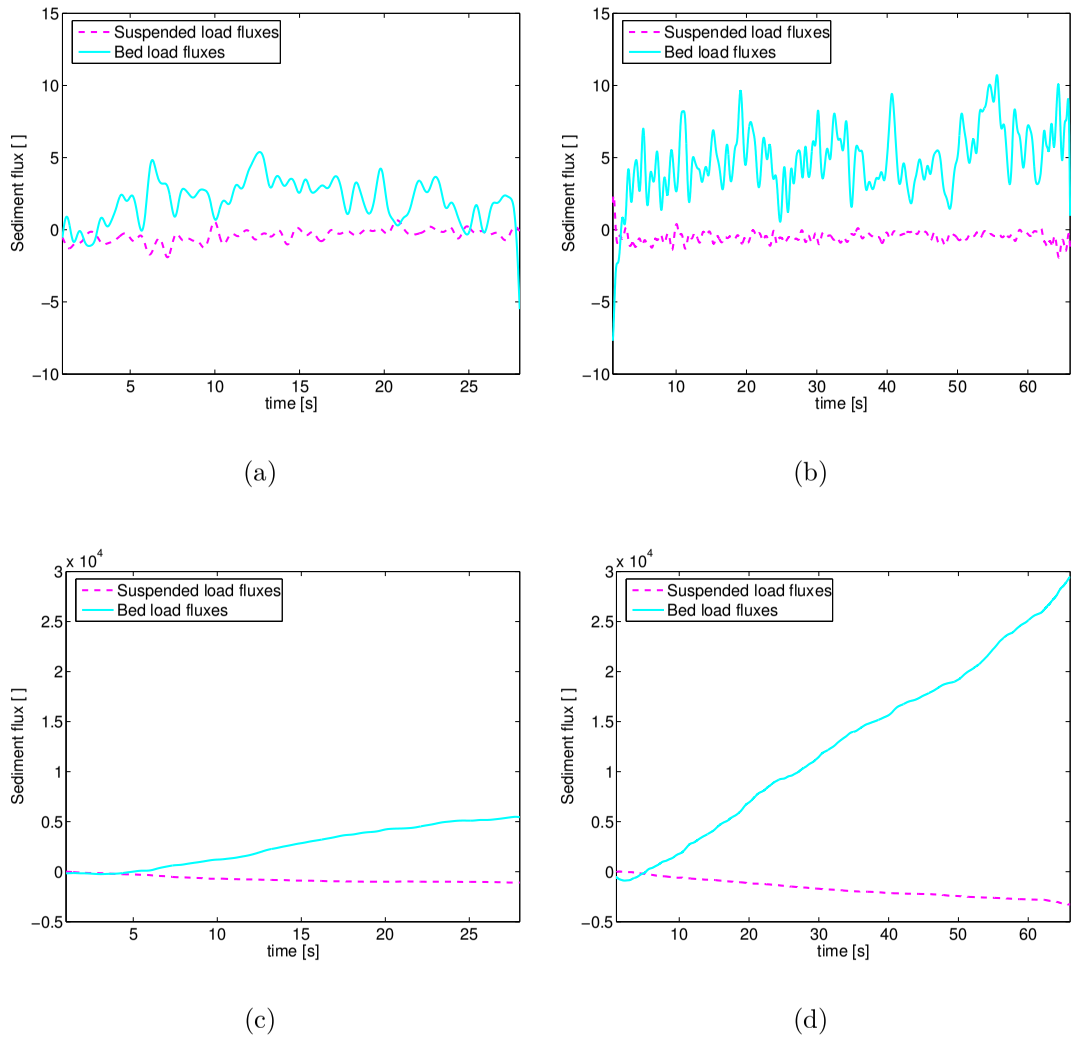

Figure 4–12. Instantaneous averaged bed and suspended load fluxes for the (a) “double-crested” ripple (E05), and (b) two-ripple (E10) cases. Cumulative averaged bed and suspended load fluxes for the (c) “double-crested” ripple (E05), and (d) two-ripple (E10) cases.

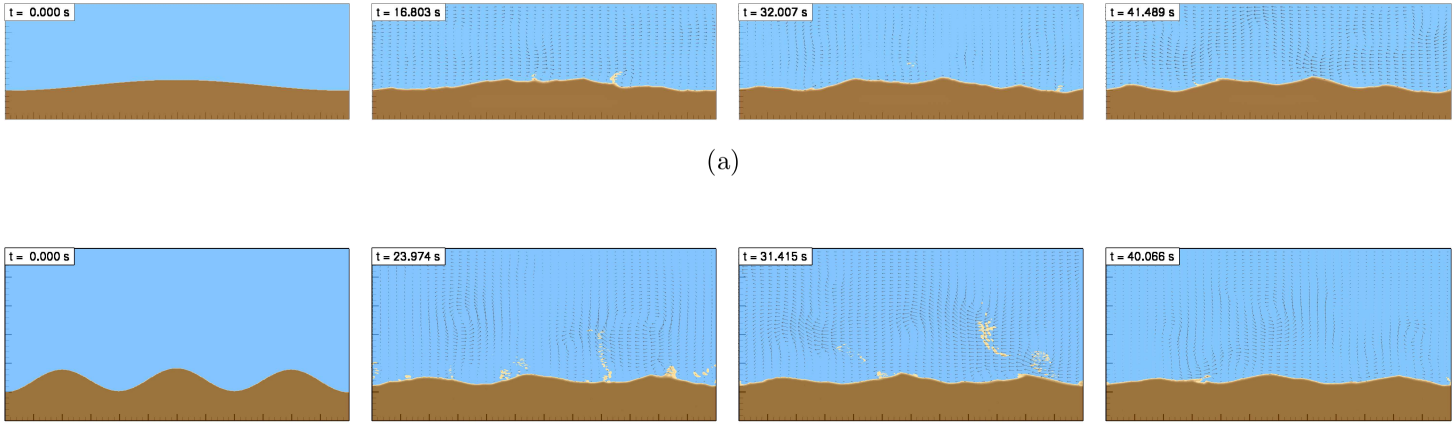

(a)

(b)

Figure 4–13. Snapshots in time of the one- and three-ripple wavelength simulations. (a) One-ripple case (E08) with $U_o = 40$ cm/s, $T = 2$ s, $\eta_o = 0.8$ cm. (b) Three-ripple case (E09) with $U_o = 40$ cm/s, $T = 2$ s, $\eta_o = 1.6$ cm.

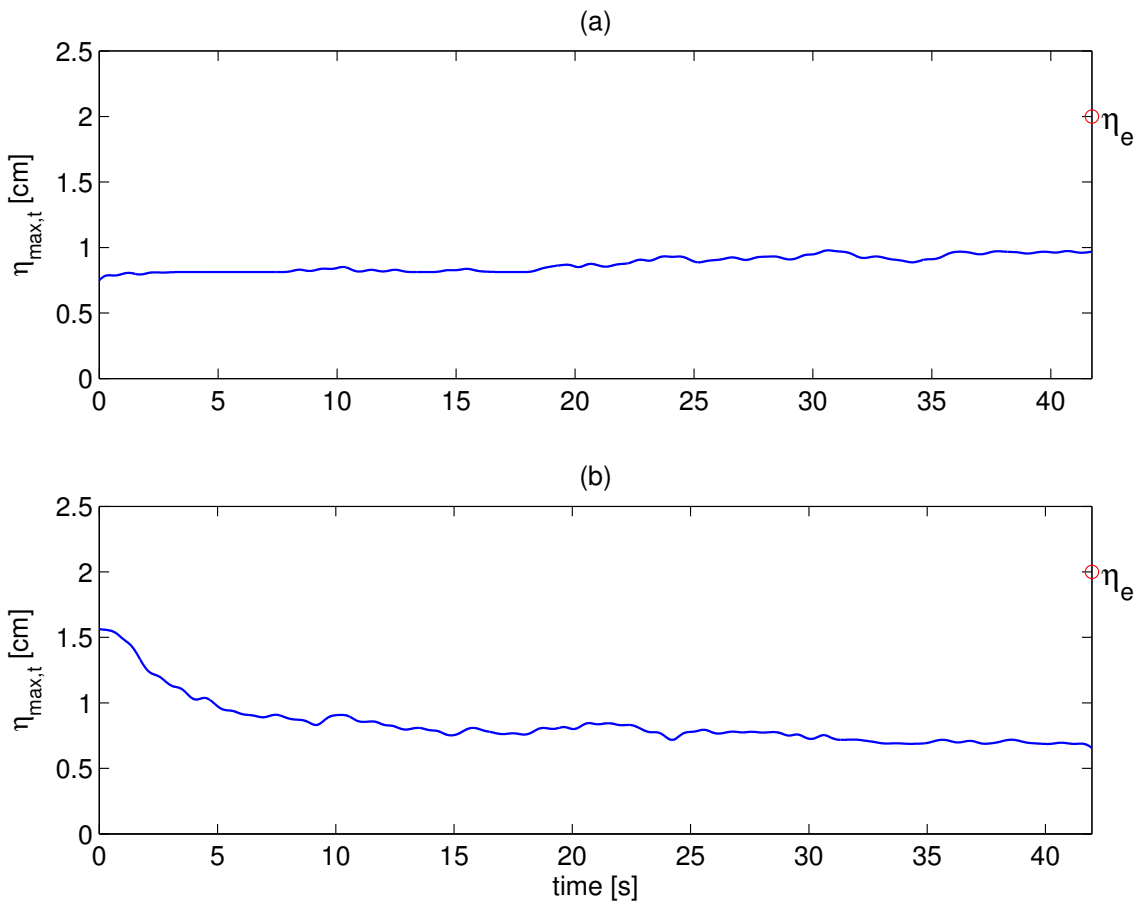

Figure 4–14. Time evolution of maximum ripple height ($\eta_{max,t}$) for the (a) one-ripple (E08), and (b) three-ripple (E09) cases. η_e denotes the equilibrium height resulting from Nielsen's steady-state formulas for the simulation conditions.

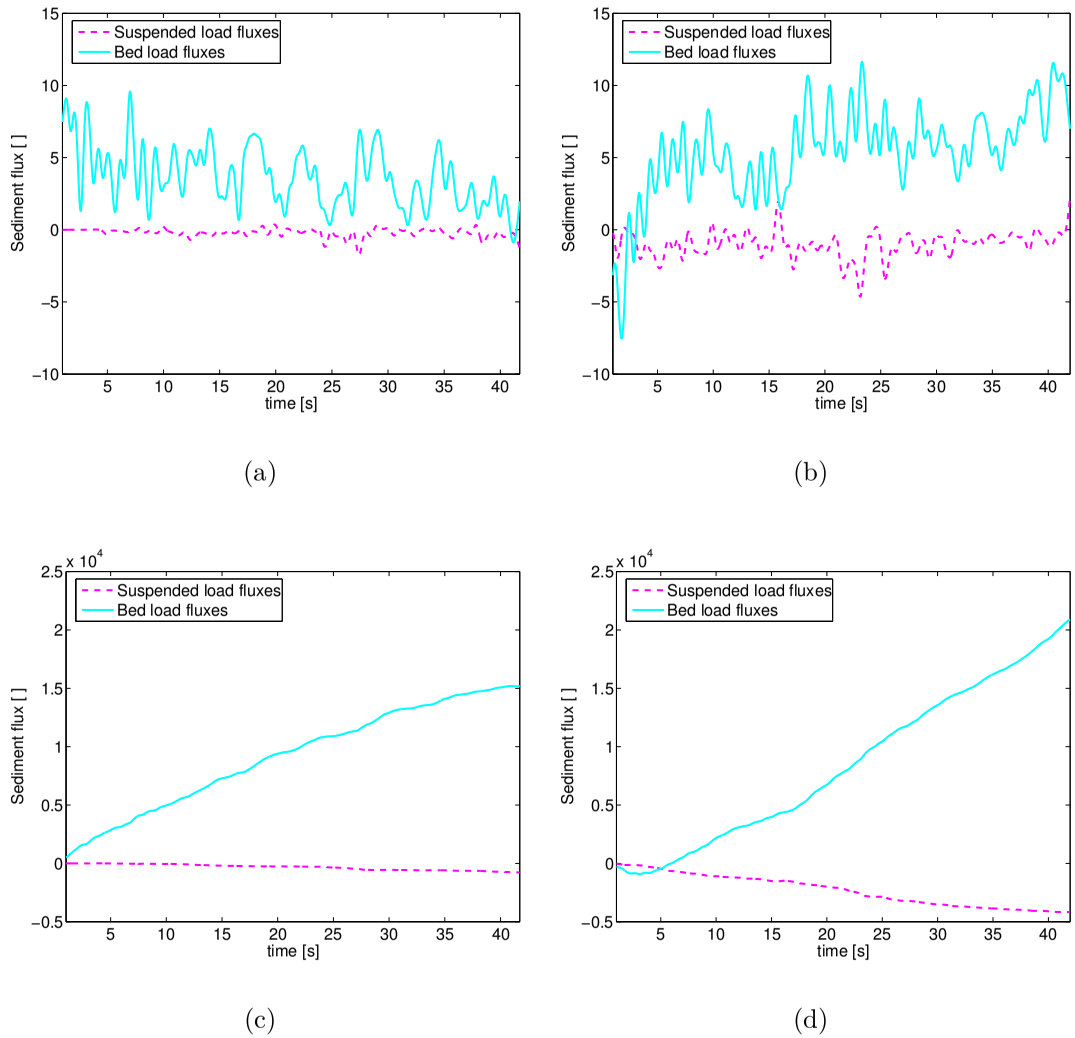

Figure 4–15. Instantaneous averaged bed and suspended load fluxes for the (a) one-ripple (E08), and (b) three-ripple (E09) cases. Cumulative averaged bed and suspended load fluxes for the (a) one-ripple (E08), and (b) three-ripple (E09) cases.

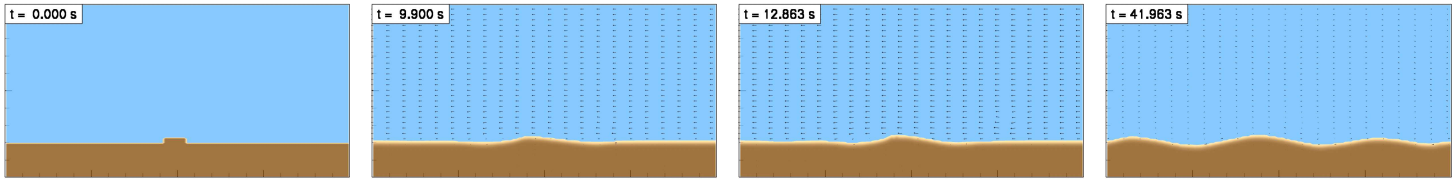

(a)

Figure 4–16. Snapshots in time of the flatbed simulation (E18) with $U_o = 20$ cm/s, $T = 1$ s, $\eta_o = 0$ cm.

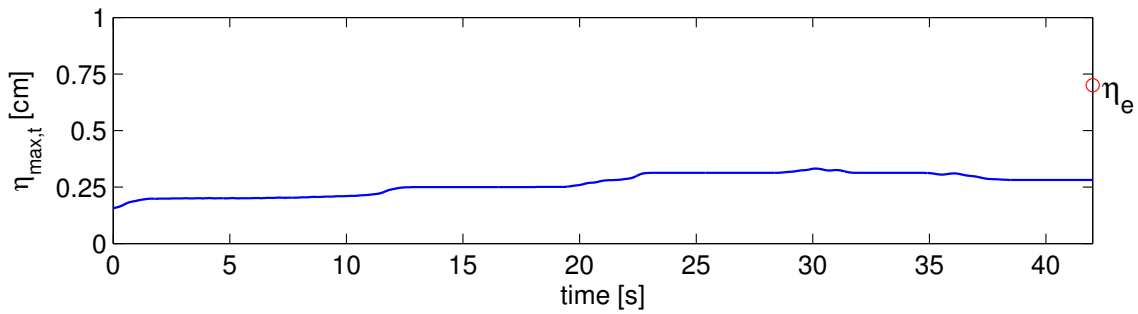

Figure 4–17. Time evolution of maximum ripple height ($\eta_{max,t}$) for the flatbed case (E18). η_e denotes the equilibrium height resulting from Nielsen's steady-state formulas for the simulation conditions.

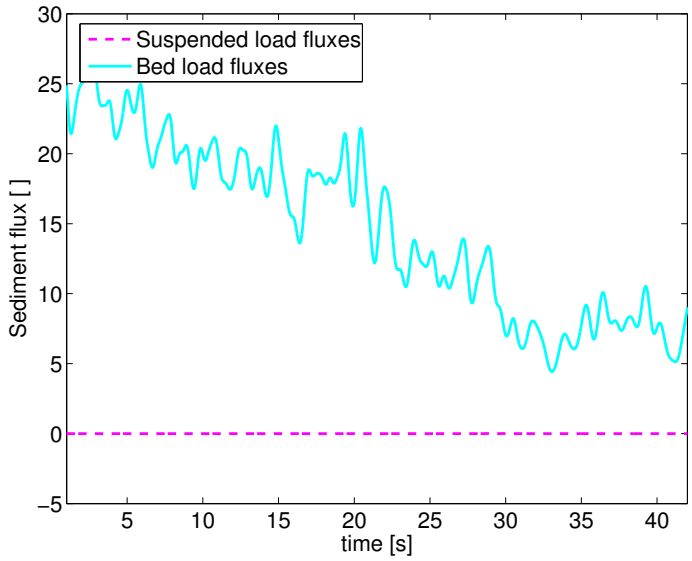

(a)

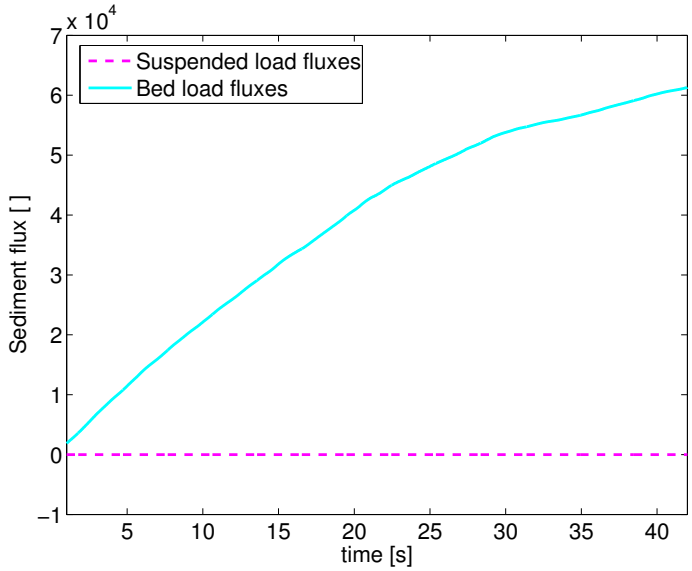

(b)

Figure 4–18. Fluxes for the flatbed simulation (E18), where (a) are the instantaneous bed and suspended load fluxes and (b) are the cumulative averaged bed and suspended load fluxes.

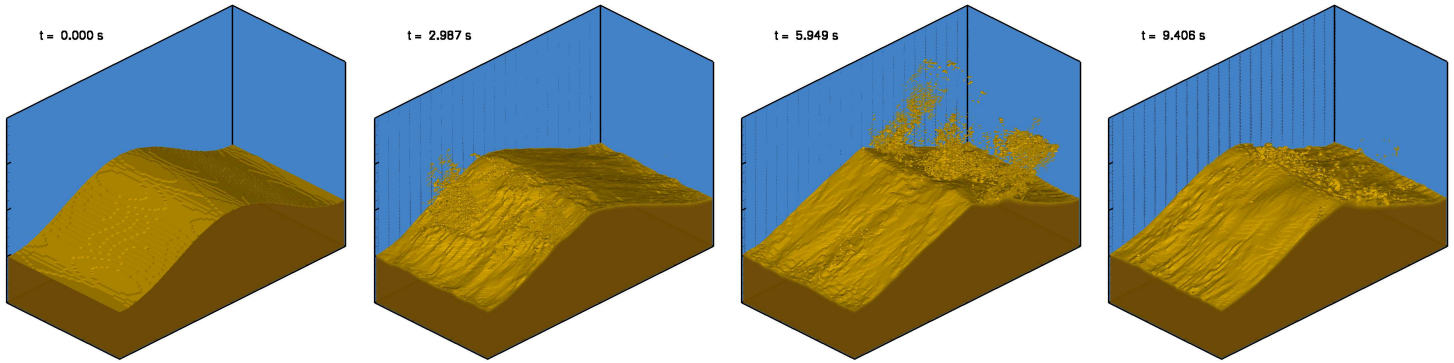

(a)

Figure 4–19. Snapshots in time of the three-dimensional simulation (E14) with $U_o = 40$ cm/s, $T = 2$ s, $\eta_o = 2$ cm.

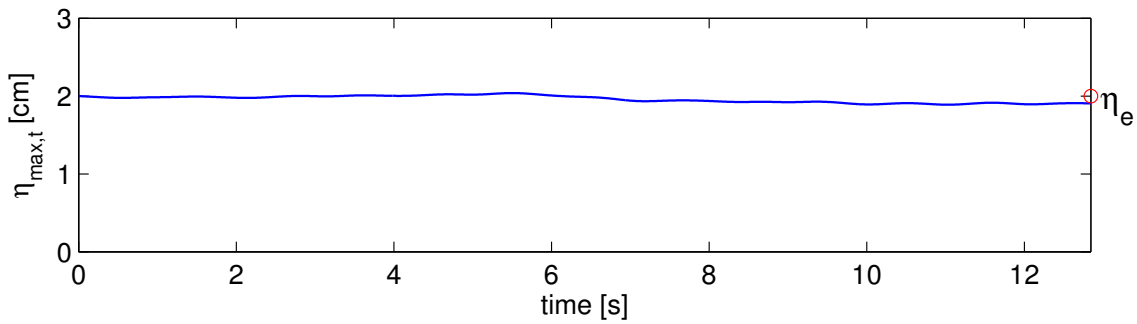

Figure 4–20. Time evolution of maximum ripple height ($\eta_{max,t}$) for the three-dimensional case (E14). η_e denotes the equilibrium height resulting from Nielsen's steady-state formulas for the simulation conditions.

Table 4–1. The initial, final, and equilibrium ripple heights for all of the presented cases.

Run name	Simulation description	Initial height (cm)	Final height (cm)	Equilibrium height (cm)	% of equilibrium height at end of simulation (%)
E03	Growing	1.0	1.5	2.0	75
DC05	Slightly decaying	2.0	1.5	2.0	75
E04	Rapidly decaying	3.0	1.5	2.0	75
E11	Low energy	2.2	0.8	1.4	57
E13	Mid energy	1.6	2.0	2.1	95
E20	High energy	1.6	0.8	0.0	N/A
E05	"Double-crested"	1.4	1.0	2.0	70
E10	Two-ripple	1.6	0.6	2.0	30
E08	One-ripple	0.8	1.0	2.0	50
E09	Three-ripple	1.6	0.7	2.0	35
E18	Flatbed	0.0	0.3	0.7	42
E14	Three-dimensional	2.0	2.0	2.0	100

Table 4–2. The initial, final, and equilibrium ripple wavelengths for all of the presented cases.

Run name	Simulation description	Initial length (cm)	Final length (cm)	Equilibrium length (cm)	% of equilibrium length at the end of simulation (%)
E05	"Double-crested"	6.0	12.0	12.0	100
E10	Two-ripple	6.0	7.0	12.0	58
E08	One-ripple	24.0	6.0	12.0	50
E09	Three-ripple	8.0	9.0	12.0	75
E18	Flatbed	0.0	2.7	4.0	67

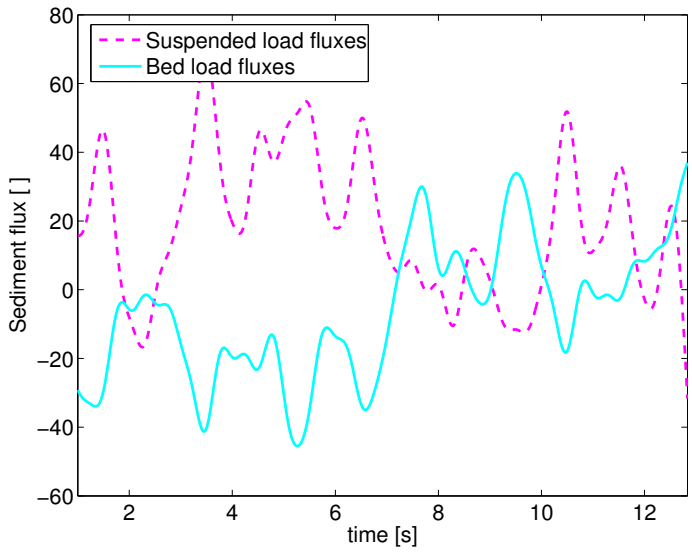

(a)

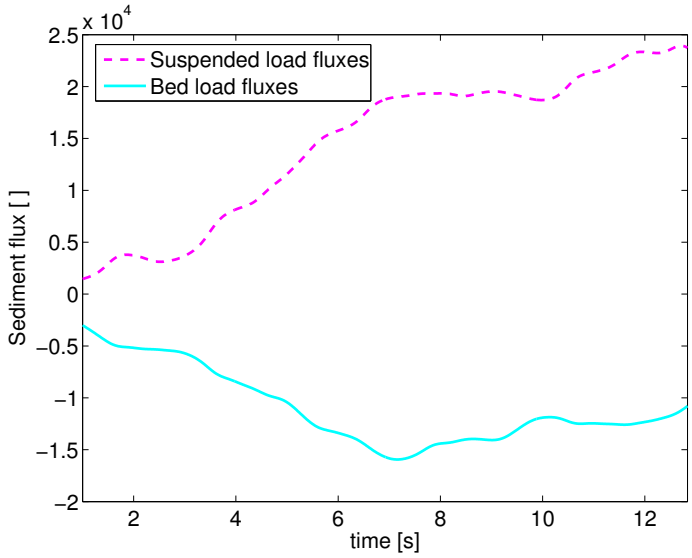

(b)

Figure 4–21. Fluxes for the three-dimensional simulation (E14), where (a) are the instantaneous bed and suspended load fluxes and (b) are the cumulative averaged bed and suspended load fluxes.

CHAPTER 5
SUMMARY

5.1 Applicability

The results of the simulations conclude that the modified mixture model of Slinn et al. (2006) is applicable to the highly concentrated, low flow, ripple regime. The model predicts realistic ripple behavior for the tested flows with Reynolds numbers ranging from 10^4 to 10^5. The model resolves the turbulent flow over a live-bed in three-dimensions. The live-bed allows for the coupled flow fields, sediment transport, and bed morphology to be analyzed. The small grid size, large number of grid points, and high resolution of the flow cause the model to be computationally expensive. The computational time required for a fully three-dimensional simulation limits the simulation domain size and duration. Further research to develop a parallel version of the code would possibly reduce the time necessary for the computations. Running the code on a supercomputer would also speed up the model run time.

5.2 Ripple Geometry Predictions

5.2.1 Ripple Shape

The ripples in the simulations are initialized with a sinusoidal shape not characteristic of those seen in nature (Haque and Mahmood, 1985). Ripples observed in the laboratory under purely oscillatory flow are generally symmetric, with narrow crests and flat, broad troughs (Wiberg and Harris, 1994). Almost immediately after the simulations begin, the sinusoidal ripple changes; the troughs become flatter and the crests become more peaked. As the simulation progresses, the peaks sway back and forth, similar to laboratory and field observations.

5.2.2 Ripple Height and Length

The simulated ripple heights and lengths were compared with Nielsen's ripple predictor method with fairly good results. When the ripple reaches its steady-state (cases E03, DC05, E04, E13, E20, and E14), the simulated ripple height comes within 75% of

the predicted height (Table 4–1). When the simulation is stopped before the ripple can reach a steady-state (cases E05 and E11), the simulated ripple height comes within 60% of the predicted height. The double-crested ripple simulation (E05) is initialized near its expected steady-state length and the simulated length equilibrates to 100% of the predicted length (Table 4–2). The simulations that have not yet reached a steady-state (cases E11, E05, E08, E09, E10, and E18) show a trend towards the equilibrium height and length. The results illustrate the model's ability to predict a steady-state ripple that is independent of the initial bed morphology. Results from the flat bed (E18) and the long flat ripple (E08) simulation agree with previous findings (e.g., Forel, 1883; Faraci and Foti, 2001) that the wavelengths of ripples initially forming on a flat bed are about half as long as the equilibrium wavelengths. The ripple geometry in these cases is not constant, illustrating that it is not yet in equilibrium. It has been found that as many as three-hundred cycles could be necessary for a flat bed to reach its equilibrium state (Faraci and Foti, 2001) and possibly more if the ripples must transition from another state (as in cases E05, E08, E09, and E10). These simulations would need to be run longer in order to make any final conclusions, although currently, the results are encouraging.

5.2.3 Ripple Morphology

Bed and suspended load transport and their contributions to ripple morphology are analyzed for each simulation. It is found that bed load transport is the dominant mechanism in ripple growth and decay. This conclusion is shown not only in the laminar flow simulation (case E18), but in all but two of the other cases. In the flat bed case, small ripples form on the initially flat bed with a small perturbation. The growth of the ripples is characterized by the rolling and sliding of grains on the lee side of the ripple which agrees with laboratory findings (Faraci and Foti, 2001). It was also found that the advective fluxes are the significant forces moving sediment. The diffusive and settling forces are in mostly in balance with each other.

5.2.4 Comparisons of Quasi-Two- and Three-Dimensional Simulations

It was found that the quasi-two-dimensional ripple amplitude simulations equilibrated to about 75% of the steady-state ripple height for the flow conditions. When the same initial flow and bed conditions were simulated in three-dimensions, the ripple height equilibrated to within 99% of the steady-state height. The differences between the quasi-two- and three-dimensional simulations can probably be attributed to increased turbulence. In the three-dimensional simulation, the turbulence is able to fully develop in the y-direction. It has been found that three-dimensional vortex structures play an important role in the transport of sediment, and higher Reynolds number flows are strongly three-dimensional (Zedler and Street, 2006). The three-dimensional vortex structures significantly affect particle trajectories and create relevant dispersion effects (Blondeaux et al., 1999; Scandura et al., 2000). From this evidence, differences between the two- and three-dimensional simulations are expected. We can conclude that in order to capture the fully resolved flow, the simulation must be run in three-dimensions. However, we can use the quasi-two-dimensional simulations to approximate the ripple morphology until the problem of computational run time is resolved.

5.3 Summary of Contributions

The purpose of this research was to determine if the sheet flow mixture model of Slinn et al. (2006) could be modified to simulate sediment transport and ripple evolution in a ripple flow regime. It is now known that the model has the capability to be useful in analyzing sediment transport and ripple morphology under flows lower than those typical of sheet flow. The model examines the live-bed dynamics of ripple evolution while fully resolving the flow. Although uncertainties associated with turbulence closure schemes are avoided due to the direct solution of the governing equations, more work must be done to experimentally verify the empirical submodels for the sediment transport dynamics. We have succeeded in creating a tool that has the potential to advance the present knowledge of coastal sediment transport and morphology.

5.4 Future Research

The computational expense of the model must first be minimized by parallelizing the code or using faster computing power. Once the simulations can be run to reach the bed's equilibrium state, the output can be better analyzed and compared to laboratory and field results. One possible comparison is Doucette and O'Donoghue's (2006) empirical model of time to ripple equilibrium. They formulated an empirical relationship dependent on the mobility number, initial ripple height, and equilibrium ripple height that determined the time dependent ripple height evolution. Unfortunately, the time scales in the formula are much longer than those currently obtained in the model. In the future, this model could also be applied to three-dimensional ripple fields, scour around objects, or bedforms in rivers with the addition of a mean current.

APPENDIX A
FLUX CALCULATIONS

The mass flux of sediment in a fluid occurs through three mechanisms: the bulk motion of the fluid, the concentration gradient, and the settling due to gravity. A sediment continuity equation (Equation A–1) that describes the movement of sediment within a fluid is derived using a mass balance of these three types of fluxes.

$$\frac{\partial C}{\partial t} = \underbrace{-\frac{\partial C u_j}{\partial x_j}}_{advective} \underbrace{-\frac{\partial C W_t}{\partial z}}_{settling} + \underbrace{\frac{\partial}{\partial x_j}\left(D_j \frac{\partial C}{\partial x_j}\right)}_{diffusion} \tag{A–1}$$

where C is the sediment concentration, u_j is the mixture velocity, W_t is the settling velocity defined by Richardson and Zaki (1954), and D_j is the diffusion coefficient defined by Nir and Acrivos (1990). The first term on the right side is the flux due to the bulk motion of the fluid, or advective flux, the second term is the flux due to settling, and the last term is the flux due to the concentration gradient (i.e., diffusion). Before calculating which fluxes contribute to ripple evolution, the processes of how a ripple grows or decays must be examined. Physically, when a ripple decays, sediment gets sheared off the peak and fills up into the trough. Because of these physical processes, both positive and negative fluxes contribute to ripple decay, and ripple growth, depending where they occur on the ripple (Figure A–1(a)). The rapidly decaying ripple case (E04) will be used as an example to show how the fluxes are calculated. In order to determine which fluxes contribute to the ripple decay in case E04, the horizontally averaged concentration profiles at two different times were plotted (Figure A–1(b)). The total contribution of the fluxes to the change in concentration between the two times is found by integrating the sediment continuity equation (Equation A–1) with respect to time.

$$\int_{t_i}^{t_f} \frac{\partial C}{\partial t} dt = C_f - C_i \tag{A–2}$$

The result of the integration is the difference between the final and the initial concentration profile (Equation A–2). This difference is plotted in Figure A–1(c). As shown in the plot, the difference between the final and initial concentration profiles is negative above the intersecting point of the two horizontally averaged concentration profiles (shown on Figure A–1(b) as the cross grid point), and positive below the intersecting point. Therefore, a positive flux below the profile intersecting point causes ripple decay. Above the intersecting point, negative fluxes contribute to the ripple decay. Figure A–1(a) illustrates this idea by the arrows denoting the direction of the decaying fluxes. This concept is also applied to a growing ripple and is opposite of the decaying ripple. Ripple growth is caused by negative fluxes below the intersecting point and positive fluxes above the profile intersecting point.

The division between bed and suspended load is defined as a set distance above the immobile bed as per previous research (Einstein, 1950). In this research, the immobile bed is defined as having a volumetric concentration of 57% or greater. The bed load layer width is then defined to be about four grain diameters thick, or ending about 0.18 cm above the immobile bed. This definition was based on visual inspection of many concentration fields (See Figure A–2 for an example). The suspended load region is the rest of the domain above the bed load layer.

The procedure for calculating which fluxes (advective, settling, or diffusive, and bed, or suspended load) contribute to ripple growth and decay is carried out as follows:

1. The initial and final averaged concentration profiles are calculated and the intersecting point between them is determined.
2. Each flux term at all grid points is calculated at every time step from the velocity and concentration output of the model.
3. The fluxes at each grid point are categorized into bed material, bed load, or suspended load depending on their location above the immobile bed as described previously.
4. The fluxes at each grid point are then determined to be contributing to ripple growth or decay depending on their sign and location relative to the intersecting concentration profile point. Growth fluxes are made positive and decay fluxes are made negative.
5. The fluxes at the grid points in the bed and suspended load regions along the ripple are summed together.

These steps yield a quantity of each of the advective, diffusive, and settling fluxes for both the bed and suspended load regions. The fluxes are plotted so positive values indicate ripple growth and negative values indicate ripple decay.

This method for calculating fluxes may not be appropriate for simulations with significantly changing ripple shapes or multi-ripple simulations. There are fluxes associated with the changing of the ripple shape that do not necessarily cause the ripple height to increase or decrease, but are counted in the growth and decay flux calculations. There is also some imprecision in the categorization of the growth and decay fluxes in relation to the profile intersection point. The intersecting profile point is calculated by averaging the initial and final concentration profiles of the simulation. If the concentration profiles are complex, or the ripples asymmetrical, the calculation of the intersecting profile point may not be accurate. In addition, the change in shape between the two times does not affect the position of the crossing point. For these reasons, the method is used to approximately determine the ripple growth and decay fluxes.

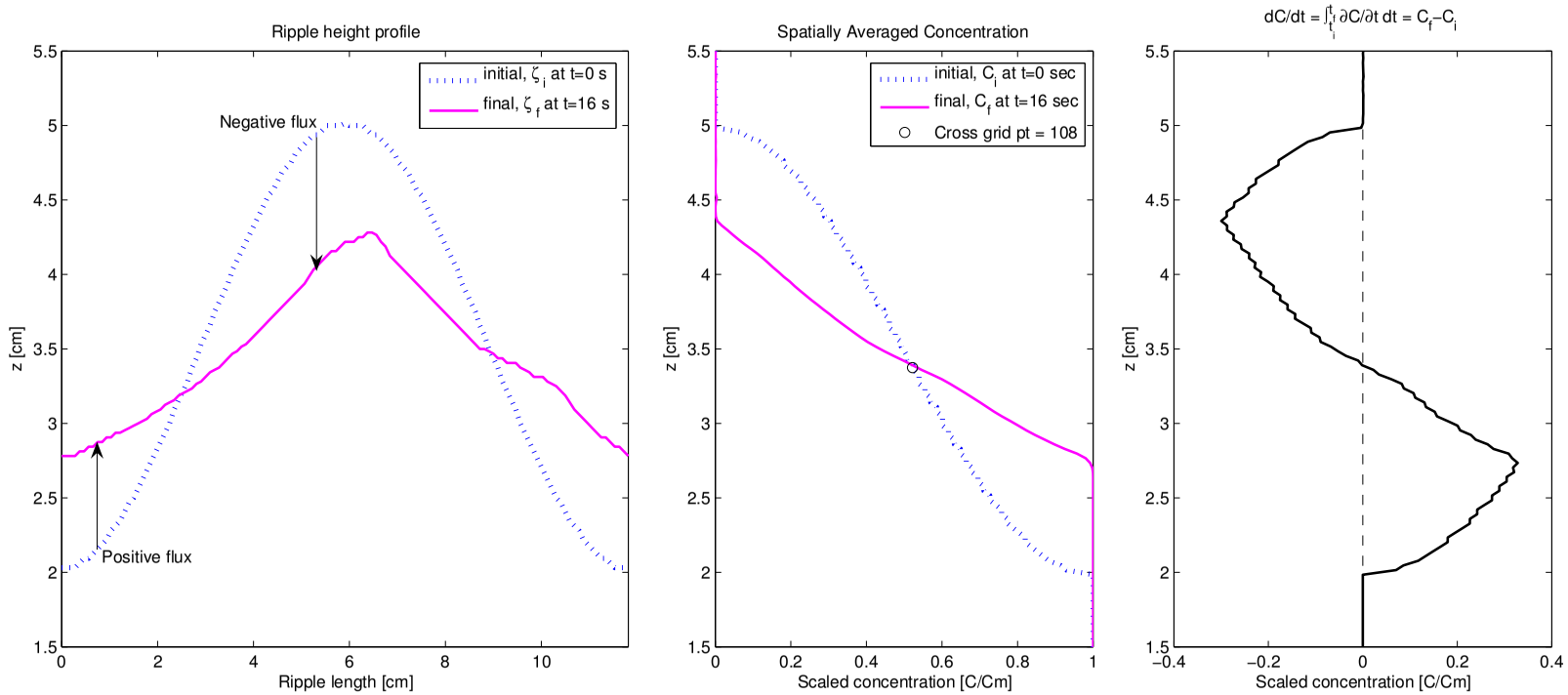

(a) (b) (c)

Figure A–1. Ripple profile and horizontally averaged concentration plots. (a) The ripple profiles at t=0 sec and t=16 sec with the arrows representing the ripple decaying fluxes. (b) The horizontally averaged concentration profiles at t=0 sec and t=16 sec, and (c) the difference between the final and initial concentrations from the rapidly decaying ripple case (E04).

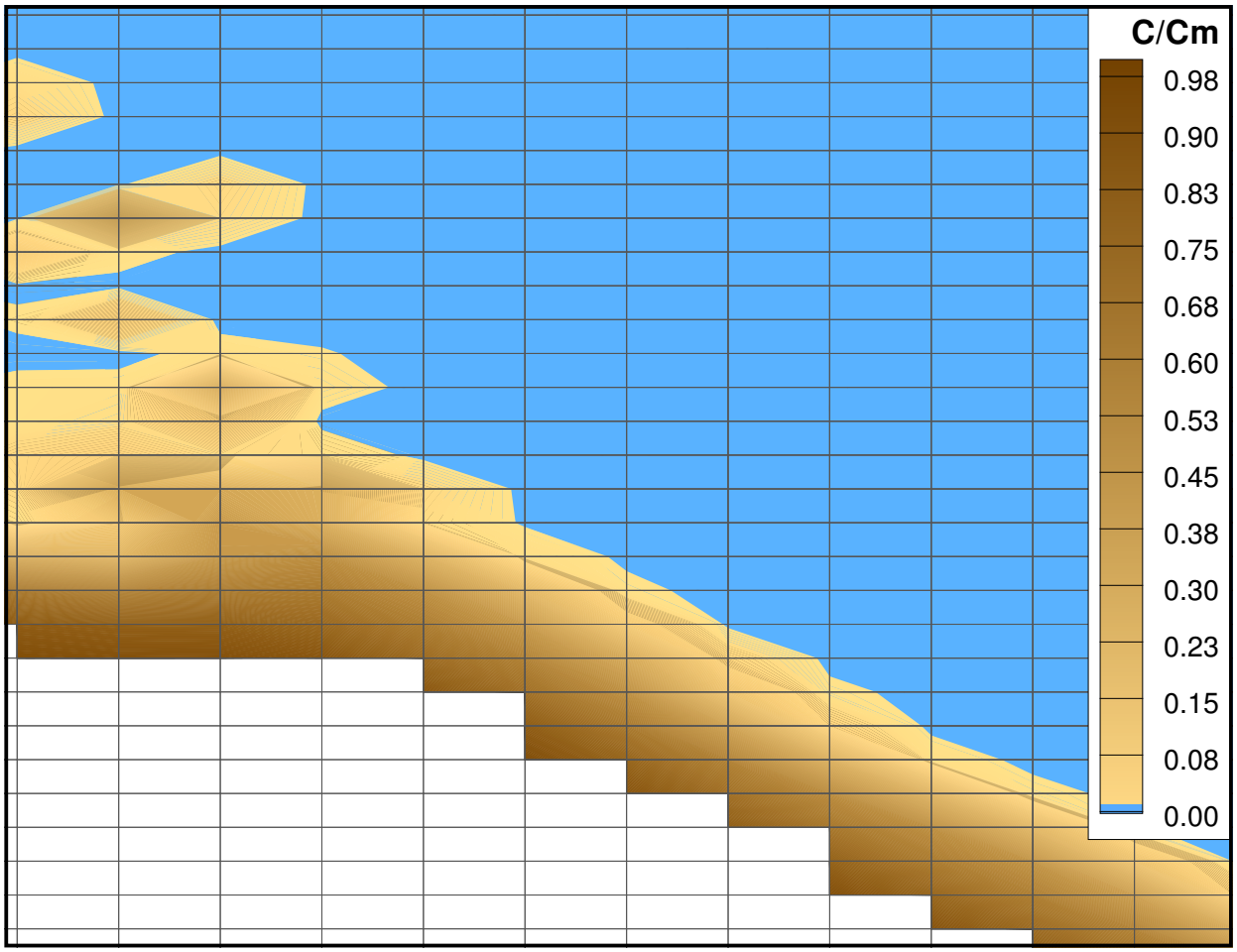

Figure A–2. A zoomed portion of the ripple surface and mesh grid. The white represents the immobile bed (C > 57% by volume). The bed load layer is six grid points thick (or 4.6d) on average.

REFERENCES

Andersen, K. H., 1999. Ripples beneath surface waves and topics in shell models of turbulence. Ph.D. thesis, Technical University of Denmark. 1.3

Andersen, K. H., 2001. A particle model of rolling grain ripples under waves. Physics of Fluids 13 (1), 58–64. 1.3, 1.4

Andersen, K. H., Chabanol, M.-L., van Hecke, M., 2001. Dynamical models for sand ripples beneath surface waves. Physical Review E (Statistical, Nonlinear, and Soft Matter Physics) 63 (6), 066308–1–066308–8. 1.3

Atkin, R. J., Craine, R. E., 1976. Continuum theories of mixtures - Basic theory and historical development. Quarterly Journal of Mechanics and Applied Mathematics 29, 209–244. 1.3

Ayrton, H., 1910. The origin and growth of ripple-mark. Proceedings of the Royal Society of London, Series A - Containing Papers of a Mathematical and Physical Character 84 (571), 285–310. 1.3

Bagnold, R. A., 1946. Motion of waves in shallow water: Interaction between waves and sand bottoms. Proceedings of the Royal Society of London, Series A 187, 1–15. 1.2, 1.2.1, 1.3

Bagnold, R. A., 1954. Experiments on a gravity-free dispersion of large solid spheres in a Newtonian fluid under shear. Proceedings of the Royal Society of London, Series A 225 (1160), 49–63. 2.2.1, 2.2.1

Bagnold, R. A., 1956. The flow of cohesionless grains in fluids. Philosophical Transactions of the Royal Society of London, Series A 249 (964), 235–297. 1.2.2

Barr, B. C., Slinn, D. N., Pierro, T., Winters, K. B., 2004. Numerical simulation of turbulent, oscillatory flow over sand ripples. Journal of Geophysical Research 109 (C9), 1–19. 1.3, 1.4

Blondeaux, P., 1990. Sand ripples under sea waves 1. Ripple formation. Journal of Fluid Mechanics 218, 1–17. 1.3

Blondeaux, P., 2001. Mechanics of coastal forms. Annual Review of Fluid Mechanics 33, 339–370. 1.3, 1.4, 3.2

Blondeaux, P., Scandura, P., Vittori, G., 1999. A lagrangian approach to describe sediment dynamics over a rippled bed: preliminary results. In: International Association of Hydraulic Research Symposium of River, Coastal, and Estuary Morphodynamics. Univ. Genova, Department of Environmental Engineering, Genova, Italy, pp. 185–194. 1.3, 5.2.4

Candolle, M. C., 1883. Rides formées archives des sciences physiques et naturelles. Archives des Sciences Physiques et Naturelles 9 (3). 1.3

Carstens, M. R., Neilson, F. M., 1967. Evolution of a duned bed under oscillatory flow. Journal of Geophysical Research 72 (12), 3053–3059. 1.3

Chang, Y. S., Hanes, D. M., 2004. Suspended sediment and hydrodynamics above mildly sloped long wave ripples. Journal of Geophysical Research 109 (C7), C07022. 1.3

Chang, Y. S., Scotti, A., 2004. Modeling unsteady turbulent flows over ripples: Reynolds-averaged Navier-Stokes equations (RANS) versus large-eddy simulation (LES). Journal of Geophysical Research 109 (C9), C09012. 1.4

Costello, W. R., Southard, J. B., 1981. Flume experiments on lower-flow-regime bed forms in coarse sand. Journal of Sedimentary Petrology 51 (3), 849–864. 1.3

Darwin, G. H., 1883. On the formation of ripple-mark in sand. Proceedings of the Royal Society of London 36, 18–43. 1.3

Davies, A. G., Ribberink, J. S., Temperville, A., Zyserman, J. A., 1997. Comparisons between sediment transport models and observations made in wave and current flows above plane beds. Coastal Engineering 31, 163–198. 1.4

Davies, A. G., van Rijn, L. C., Damgaard, J. S., van de Graaff, J., Ribberink, J. S., 2002. Intercomparison of research and practical sand transport models. Coastal Engineering 46, 1–23. 1.4

Dingler, J., 1974. Wave formed ripples in nearshore sands. Ph.D. thesis, University of California, San Diego. 1.3

Dohmen-Janssen, C. M., Hassan, W. N., Ribberink, J. S., 2001. Mobile-bed effects in oscillatory sheet flow. Journal of Geophysical Research 106 (C11), 27103–27115. 1.3, 1.4

Doucette, J. S., 2002. Geometry and grain-size sorting of ripples on low-energy sandy beaches: field observations and model predictions. Sedimentology 49 (3), 483–503. 1.3, 1.4

Doucette, J. S., O'Donoghue, T., 2006. Response of sand ripples to change in oscillatory flow. Sedimentology 53 (3), 581–596. 1.3, 5.4

Drew, D. A., 1975. Turbulent sediment transport over a flat bottom using momentum balance. Journal of Applied Mechanics - Transactions of ASME 42 (1), 38–44. 1.3

Drew, D. A., 1983. Mathematical-modeling of two-phase flow. Annual Review of Fluid Mechanics 15, 261–291. 1.3, 2.2.1, 2.2.1

Eidsvik, K. J., 2004. Some contributions to the uncertainty of sediment transport predictions. Continental Shelf Research 24 (6), 739–754. 1.3

Einstein, A., 1906. Eine neue Bestimmung der Moleküldimensionen (German) [A new determination of molecular dimensions]. Annalen der Physik 19, 289–306. 1.3

Einstein, H. A., 1950. The bed-load function for sediment transportation in open channel flows. Technical Bulletin 1026, U. S. Department of Agriculture. 1.2.2, A

Faraci, C., Foti, E., 2001. Evolution of small scale regular patterns generated by waves propagating over a sandy bottom. Physics of Fluids 13 (6), 1624–1634. 1.3, 5.2.2, 5.2.3

Faraci, C., Foti, E., 2002. Geometry, migration and evolution of small-scale bedforms generated by regular and irregular waves. Coastal Engineering 47, 35–52. 1.3, 1.4, 3.2

Forel, M., 1883. Les rides de fond. Archives des Sciences Physiques et Naturelles. 1.3, 5.2.2

Foti, E., Blondeaux, P., 1995. Sea ripple formation - The turbulent boundary-layer case. Coastal Engineering 25, 227–236. 1.3

Fredsøe, J., Deigaard, R., 1992. Mechanics of Coastal Sediment Transport. World Scientific, Singapore. 1.2.1, 1.2.2, 2.2.1

Grant, W. D., Madsen, O. S., 1979. Combined wave and current interaction with a rough bottom. Journal of Geophysical Research 84 (C4), 1797–1808. 1.3

Grant, W. D., Madsen, O. S., 1982. Movable bed roughness in unsteady oscillatory flow. Journal of Geophysical Research 87 (C1), 469–481. 1.3, 4.4.1

Grant, W. D., Madsen, O. S., 1986. The continental-shelf bottom boundary-layer. Annual Review of Fluid Mechanics 18, 265–305. 1.3

Grasmeijer, B. T., Kleinhans, M. G., 2004. Observed and predicted bedforms and their effect on suspended sand concentrations. Coastal Engineering 51, 351–371. 1.3, 1.4, 3.2

Guizien, K., Dohmen-Janssen, M., Vittori, G., 2003. 1DV bottom boundary layer modeling under combined wave and current: Turbulent separation and phase lag effects. Journal of Geophysical Research 108 (C1), 3016. 1.3

Hanes, D. M., Alymov, V., Chang, Y., Jette, C., 2001. Wave-formed sand ripples at Duck, North Carolina. Journal of Geophysical Research 106 (C10), 22575–22592. 1.3

Hansen, E. A., Fredsoe, J., Deigaard, R., 1994. Distribution of suspended sediment over wave-generated ripples. Journal of Waterway, Port, Coastal, and Ocean Engineering 120 (1), 37–55. 1.3

Haque, M. I., Mahmood, K., 1985. Geometry of ripples and dunes. Journal of Hydraulic Engineering 111 (1), 48–63. 5.2.1

Hara, T., Mei, C. C., Shum, K. T., 1992. Oscillating flows over periodic ripples of finite slope. Physics of Fluids A-Fluid Dynamics 4 (7), 1373–1384. 1.3

Hsu, T. J., Jenkins, J. T., Liu, P. L. F., 2004. On two-phase sediment transport: sheet flow of massive particles. Proceedings of the Royal Society of London, Series A - Mathematical Physical and Engineering Sciences 460 (2048), 2223–2250. 1.3, 1.4

Hunt, A. R., 1882. On the formation of ripplemark. Proceedings of the Royal Society of London 34, 1–18. 1.3

Hunt, M., Zenit, R., Campbell, C., Brennen, C., 2002. Revisiting the 1954 suspension experiments of R. A. Bagnold. Journal of Fluid Mechanics 452, 1–24. 2.2.1

Inman, D., 1957. Wave generated ripples in nearshore sands. Technical Memo 100, Beach Erosion Board. 1.3

Jenkins, J. T., Hanes, D. M., 1998. Collisional sheet flows of sediment driven by a turbulent fluid. Journal of Fluid Mechanics 370, 29–52. 2.2.1

Ji, S. B., Gerber, A. G., Sousa, A. C. M., 2004. A convection-diffusion CFD model for aeolian particle transport. International Journal for Numerical Methods in Fluids 45 (8), 797–817. 1.3

Khelifa, A., Ouellet, Y., 2000. Prediction of sand ripple geometry under waves and currents. Journal of Waterway, Port, Coastal, and Ocean Engineering 126 (1), 14–22. 1.4

Lee, T. H., Hanes, D. M., 1996. Comparison of field observations of the vertical distribution of suspended sand and its prediction by models. Journal of Geophysical Research 101 (C2), 3561–3572. 1.3, 1.4

Leighton, D., Acrivos, A., 1986. Viscous resuspension. Chemical Engineering Science 41 (6), 1377–1384. 2.2.1, 2.2.1, 2.2.1, 2.2.1

Leighton, D., Acrivos, A., 1987. The shear-induced migration of particles in concentrated suspensions. Journal of Fluid Mechanics 181, 415–439. 2.2.1

Li, M. Z., Amos, C. L., 1998. Predicting ripple geometry and bed roughness under combined waves and currents in a continental shelf environment. Continental Shelf Research 18 (9), 941–970. 1.3, 1.4

Li, M. Z., Amos, C. L., 2001. SEDTRANS96: the upgraded and better calibrated sediment-transport model for continental shelves. Computers & Geosciences 27 (6), 619–645. 1.3

Lofquist, K., 1978. Sand ripple growth in an oscillatory-flow water tunnel. Technical Memo 78-5, Coastal Engineering Research Center. 1.3

Longuet-Higgins, M., 1981. Oscillating flow over steep sand ripples. Journal of Fluid Mechanics 107, 1–35. 1.3

McTigue, D. F., 1981. Mixture theory for suspended sediment transport. Journal of the Hydraulics Division 107 (6), 659–673. 1.3, 1.4

Miller, M. C., Komar, P. D., 1980a. A field investigation of the relationship between oscillation ripple spacing and the near-bottom water orbital motions. Journal of Sedimentary Petrology 50 (1), 183–191. 1.3

Miller, M. C., Komar, P. D., 1980b. Oscillation sand ripples generated by laboratory apparatus. Journal of Sedimentary Petrology 50 (1), 173–182. 1.3

Mogridge, G., Davies, M., Willis, D., 1994. Geometry prediction for wave-generated bedforms. Coastal Engineering 22, 255–286. 1.3

Mogridge, G. R., Kamphuis, J. W., 1972. Experiments on bed form generation by wave action. In: Proceedings of the 13th International Conference on Coastal Engineering. Vol. 2. Vancouver, BC, pp. 1123–1142. 1.2.3, 1.3, 3.2

Nielsen, P., 1981. Dynamics and geometry of wave generated ripples. Journal of Geophysical Research 86 (C7), 6467–6472. 1.3, 3.1, 3.2, 3.2, 3.2, 3–4, 4.1.1, 4.2.2, 4.3.1, 4.6.1, 4–2, 4–8, 4–11, 4–14, 4–17, 4–20, 5.2.2

Nielsen, P., 1992. Coastal Bottom Boundary Layers and Sediment Transport. World Scientific, Singapore. 1.2, 1.2.1, 1.3

Nir, A., Acrivos, A., 1990. Sedimentation and sediment flow on inclined surfaces. Journal of Fluid Mechanics 212, 139–153. 2.2.1, A

O'Donoghue, T., Clubb, G. S., 2001. Sand ripples generated by regular oscillatory flow. Coastal Engineering 44, 101–115. 1.3, 1.4, 4.4.1

O'Donoghue, T., Doucette, J., van der Werf, J., Ribberink, J., 2006. The dimensions of sand ripples in full-scale oscillatory flows. Coastal Engineering 53, 997–1012. 1.3, 1.4, 3.2

Phillips, R. J., Armstrong, R. C., Brown, R. A., Graham, A. L., Abbott, J. R., 1992. A constitutive equation for concentrated suspensions that accounts for shear-induced particle migration. Physics of Fluids A-Fluid Dynamics 4 (1), 30–40. 1.3, 2.2.1

Piper, J. E., Commander, K. W., Thorsos, E. I., Williams, K. L., 2002. Detection of buried targets using a synthetic aperture sonar. IEEE Journal of Oceanic Engineering 27 (3), 495–504. 1.1

Ribberink, J. S., Al-Salem, A. A., 1995. Sheet flow and suspension of sand in oscillatory boundary layers. Coastal Engineering 25 (3), 205–225. 1.3, 1.4

Richardson, J. F., Zaki, W. N., 1954. The sedimentation of a suspension of uniform spheres under conditions of viscous flow. Chemical Engineering Science 3, 65–73. 2.2.1, 2.2.1, A

Scandura, P., Vittori, G., Blondeaux, P., 2000. Three-dimensional oscillatory flow over steep ripples. Journal of Fluid Mechanics 412, 355–378. 1.3, 5.2.4

Schmidt, H., Lee, J. Y., 1999. Physics of 3-D scattering from rippled seabeds and buried targets in shallow water. Journal of the Acoustical Society of America 105 (3), 1605–1617. 1.1

Sleath, J., 1984. Sea Bed Mechanics. Wiley, New York. 1.2, 1.2.1, 1.2.2, 1.3

Sleath, J. F. A., 1976. On rolling grain ripples. Journal of Hydraulic Research 14 (1), 69–81. 1.3

Slinn, D., Hesser, T., Burdick, G., 2006. Modeling sediment transport in oscillatory boundary layers using a mixture approach. In: Eos Trans. AGU. Vol. 87 of Ocean Sciences Meeting Supplement, Abstract OS44N-01. 2.2, 5.1, 5.3

Soo, S. L., 1978. Diffusion in mulitphase flow. Iranian Journal of Science and Technology 7 (5), 31–35. 1.3

Soo, S. L., Tung, S. K., 1972. Deposition and entrainment in pipe-flow of a suspension. Powder Technology 6 (5), 283–294. 1.3

Subia, S. R., Ingber, M. S., Mondy, L. A., Altobelli, S. A., Graham, A. L., 1998. Modelling of concentrated suspensions using a continuum constitutive equation. Journal of Fluid Mechanics 373, 193–219. 1.3, 1.4

Swart, D. H., 1974. Offshore sediment transport and equilibrium beach profiles. Delft Hydraulics Publication, vol. 131. Delft Hydraulics, The Netherlands. 1.2.3

Trouw, K., Williams, J. J., Rose, C. P., 2000. Modelling sand resuspension by waves over a rippled bed. Estuarine Coastal and Shelf Science 50 (1), 143–151. 1.3

Trowbridge, J., Madsen, O. S., 1984. Turbulent wave boundary-layers 1. Model formulation and 1st-order solution. Journal of Geophysical Research 89 (C5), 7989–7997. 1.3

van der Werf, J. J., Ribberink, J. S., O'Donoghue, T., Doucette, J. S., 2006. Modelling and measurement of sand transport processes over full-scale ripples in oscillatory flow. Coastal Engineering 53 (8), 657–673. 1.2.2

Vittori, G., Blondeaux, P., 1990. Sand ripples under sea waves 2. Finite-amplitude development. Journal of Fluid Mechanics 218, 19–39. 1.3

Vongvisessomjai, S., 1984. Oscillatory ripple geometry. Journal of Hydraulic Engineering 110 (3), 247–266. 1.3

Watanabe, Y., Matsumoto, S., Saeki, H., 2003. Three-dimensional boundary layer flow over ripples. In: Proceedings from Coastal Sediments 2003. (CD-ROM). 1.3, 1.4

Wiberg, P. L., Harris, C. K., 1994. Ripple geometry in wave-dominated environments. Journal of Geophysical Research 99, 775–789. 1.2, 1.2.1, 1.3, 5.2.1

Wikramanayake, P., 1993. Velocity profiles and suspended sediment transport in wave-current flows. Ph.D. thesis, Massachusetts Institute of Technology. 1.3

Wilcox, D., 1998. Turbulence Modeling for CFD, 2nd Edition. DCW Industries, La Cañada, California. 1.3

Williams, J. J., Bell, P. S., Thorne, P. D., Metje, N., Coates, L. E., 2004. Measurement and prediction of wave-generated suborbital ripples. Journal of Geophysical Research 109 (C2), C02004. 1.3

Zedler, E. A., Street, R. L., 2006. Sediment transport over ripples in oscillatory flow. Journal of Hydraulic Engineering 132 (2), 180–193. 1.3, 1.4, 5.2.4

BIOGRAPHICAL SKETCH

I grew up on the shores of Lake Erie in Euclid, Ohio, a suburb of Cleveland, Ohio. Living near a lake induced a fascination with water and beaches which has grown into my lifelong career. I played on the beach, swam, or sailed on Lake Erie almost every day during the summer from the age of two until high school.

In grade school I was drawn to the subjects of math and science, although I enjoyed all aspects of my education. My tendency toward quantitative analysis increased in high school and was the basis of my pursuit of engineering in college. I graduated Valedictorian in a class of 500 from Euclid High School in June of 2000 and enrolled at The Ohio State University three months later. I declared my major as engineering, a specialization undecided, but quickly found an interest in civil engineering and fluid dynamics. One of my professors, Dr. Diane Foster, introduced me to coastal engineering in a water resource engineering class. In 2003, I received a full scholarship and stipend to do undergraduate research in the area of my choice. I began studying small-scale sediment transport modeling with Dr. Foster the summer of 2003. She became a very important mentor and was the fundamental inspiration in my goal to become a college professor. In September of 2003, I had the opportunity to participate in NCEX, an extensive field experiment at Scripps Institution of Oceanography in San Diego, California. The experience showed me the field aspect of coastal engineering. In addition to participating in coastal research and schoolwork, I was also an officer in Ohio State's Society of Women Engineering chapter, an active member of Women in Engineering, an undergraduate teaching assistant, and was inducted into numerous honor's societies throughout my undergraduate career.

My desire to work toward an advanced degree was motivated by a dream of working in academia. In August of 2004, I packed up my life, left the only home I had ever known, and made the 900 mile move down to Gainesville, where I would attend graduate school at the University of Florida. I have had many incredible career opportunities at UF. My first semester I participated in two research cruises to investigate sand ripples for the Ripple

DRI project. In June 2005, I traveled to Oregon for 2 weeks to take part in CROSSTEX, a large laboratory experiment at the O. H. Hinsdale Research Laboratory at Oregon State University. I have continued my research in sediment transport the past two years working with Dr. Don Slinn. After finishing my master's research, I plan to continue and work toward a Ph.D. in coastal engineering at the University of Florida.